Femtosecond Laser Ablation of Si, GaAs and InP

by

ANDRZEJ BOROWIEC, B.Sc.

A Thesis

Submitted to the School of Graduate Studies

In Partial Fulfillment of the Requirements

for the Degree

Master of Engineering

McMaster University

MASTER OF ENGINEERING (2000)   MaMaster
(Engineering Physics)   University
                                        Hamilton, Ontario

TITLE: Femtosecond Laser Ablation of Si, GaAs and InP

AUTHOR: Andrzej Borowiec, B. Sc. (Lakehead University)

SUPERVISOR: Professor Harold K. Haugen

NUMBER OF PAGES: viii, 80

Abstract

This thesis presents the study of x-ray emission from femtosecond laser micromachining and laser ablation of semiconductors. Prior to femtosecond machining experiments we investigated the nature of radiation emitted during the irradiation of solid targets with 120 femtosecond pulses with energies between 500 nJ and 0.3 mJ at a 1 kHz repetition rate. We have shown that the majority of the radiation was emitted below 10 keV with the high energy edge extending up to 25 keV. Under our experimental conditions K line emission was observed from materials with $Z < 32$. We have also measured the x-ray dose rates during laser machining of various targets on the order of 10 mSv/h at a distance of 13 cm from the target. The implications for work pace safety, micromachining control and potential for pulsed x-ray line sources for spectroscopic and imaging applications are discussed.

In our studies of single shot femtosecond ablation of selected semiconductors: Si, GaAs, and InP, we have concentrated on the studies of microstructure and composition of the material after irradiation with 120 femtosecond pulses with energies between 2 nJ and 2 μJ. The resulting surface morphology, structure and composition of the micron scale ablation features on the semiconductors were studied by electron microscopy and atomic force microscopy. We found that no sharp threshold in the surface morphology was observed with increasing pulse power; however three ablation stages were identified based on the characteristic features of the ablation craters. TEM analysis revealed essentially no crystal damage beneath and in the vicinity of the ablation craters. In case of the binary semiconductors 5-30 nm polycrystalline grains were found over the ablated surface. The results were discussed in terms of the existing state of knowledge of ablation dynamics. The implications for practical micromachining applications are also discussed.

Acknowledgements

I would like to express my thanks and gratitude to my supervisor Dr. Harold Haugen for giving me a chance to work on this exciting and challenging project as well as for his guidance and valuable discussion. Harold has given me a lot of freedom to explore my own ideas and directions; at the same time he was _always_ ready to help with practical problems, analysis and interpretation of result.

Secondly, I would like to thank Dr. Jan Thøgersen who has been my lab mentor especially in the areas of lasers and optics. Jan also deserves a lot, if not all the credit for stimulating and pushing our work on x-ray emission from laser micromachining, pulse compression, THz generation and spectroscopy, and pump-probe spectroscopy. His enthusiasm and passion for science an was inspiration for us all.

I also would like to thank Dr. George Weatherly, Dr. Maurine McKenzie and Andy Duft for their help with preparation and analysis of the TEM and AFM samples. Their help and expertise were invaluable in studies of femtosecond laser ablation of semiconductors.

Finally I would like to acknowledge my laboratory colleagues Dr. Henry Tiedje, Steve Wallace and Mike Brennan for their advice, help and valuable discussion during the course of my graduate work.

Contents

List of Figures

Chapter 1

Introduction

1.1 Introduction

The terms ultrafast and ultrashort have different meanings in different areas of science and technology. Although there is no precise definition, in the context of laser physics ultrafast or ultrashort refers to the subset of pulsed lasers capable of producing femtosecond light pulses (1 fs = 10^{-15} s). Ultrafast laser technology has taken on a whole new meaning during the past decade with laser pulses duration approaching 4.5 fs. To put the timescales involved in perspective, one can note that a 4.5 fs pulse consists of only three optical cycles in the near infrared (at 800 nm) and extends only 1.5 µm in free space. During the course of my Master's degree our laser system has been operating for 1600 hours. The sum of all pulses emitted during that time adds up to 800 µs of continuous beam time.

Ultrafast lasers have a number of unique characteristics. First of all very high peak powers can be achieved since the pulse energy is delivered in an extremely short duration. For example, a 10 mJ, 10 fs pulse focused to the diffraction limit (spot size on the order of 1 µm) leads to a focal volume on the order of 10^{-11} cm^3 and energy densities on the order of

10^9 J/cm^3, equivalent to the chemical energy of 2 tons of TNT/cm^3. Such enormous intensities grant easy access to a variety of nonlinear processes. Ultrashort pulses are also inherently broadband in nature. For example, a 10 fs pulse has a spectral bandwidth of 100 nm (100 THz). Such bandwidth is often associated with white light sources; however, ultrashort pulses offer much higher spectral brightness, especially for spectroscopic applications.

The unique characteristics of ultrashort pulses have opened new possibilities in numerous areas of science and technology. Pump-probe techniques allow spectroscopic investigations of chemical reactions, molecular dynamics, carrier dynamics in semiconductors, and other phenomena, which take place on the femtosecond time scale. Ultrafast lasers are also used to generate extreme wavelengths from THz radiation, far infrared, vacuum ultraviolet, soft and hard x-ray radiation. The applications in imaging, such as two-photon confocal microscopy, have become standard tools in many laboratories. Micromachining and micro-modification of materials is also an area of intense research since ultrafast machining has been shown to yield superior results compared to conventional lasers. In fact, femtosecond micromachining work stations have already appeared on the market. Despite the industrial interest in this technology, the details of laser-matter interaction associated with femtosecond laser machining are still not completely understood.

1.2 Thesis Outline

The work presented in this Master's thesis was completed at McMaster University between September 1998 and 2000 under the supervision of Dr. Harold K. Haugen. The first part of the project included setting up the laser system, building the necessary diagnostic tools and experimental apparatus, and writing control and acquisition software. Two major sets of experiments were then performed: the characterization of hard radiation resulting from laser micromachining of solid targets, and the analysis of material after irradiation with single femtosecond pulses.

The thesis is divided into three main chapters. Chapter 2 presents an overview of the ultrafast laser theory, as well as mathematical tools used to describe and model the formation and propagation of ultrashort optical pulses. The second section of chapter 2 outlines the basic components and specifications of our amplified femtosecond laser system. The last section of chapter 2 presents the experimental tools used to characterize ultrafast laser pulses and beam properties. Chapter 3 relates experimental details and results of the experiments associated with x-ray emission from femtosecond laser micromachining. Prior to femtosecond machining experiments we investigated the nature of radiation emitted during the irradiation of solid targets with 120 femtosecond pulses with energies between 500 nJ and 0.3 mJ at 1kHz repetition rate. The implications for workplace safety, micromachining control and laser based x-ray sources are contained in the discussion. Chapter 4 contains details of our preliminary studies of single shot femtosecond ablation of selected technologically relevant semiconductors: Si, GaAs, and InP. Analysis of the laser machined samples was performed with various microscopic and spectroscopic techniques. Chapter 5

includes the final conclusions and a discussion of the possibilities for extended work in the

area of femtosecond laser micromachining.

Chapter 2

Femtosecond Laser Pulses

This chapter will present the basic concepts and mathematical tools used to describe the formation and propagation of femtosecond laser pulses in matter. This discussion follows references [1] and [2]. The basic structure of femtosecond oscillators and the principles of ultrafast laser pulse amplification are discussed in the second section. The final section presents an overview of pulse diagnostic techniques.

2.1 Theoretical framework

2.1.1 Introduction

The majority of ultrafast lasers rely on the process of mode-locking to generate short optical pulses. The term mode-locking originates from the description of the pulse formation process in the frequency domain. A typical free running laser cavity can operate on as many as ~100,000 longitudinal modes. The exact number of modes depends on the bandwidth of the gain medium and the cavity geometry. If there is no fixed phase relationship between the cavity modes, the laser output will be continuous wave (cw) emission. However, if the cavity modes are phase locked they will add coherently and interfere constructively only in

one point in time (T = 0) and destructively everywhere else. The output of a modelocked laser is then a train of short, intense pulses separated temporally by the cavity round trip time. The principle of mode-locking is illustrated in the figure below. The top portion of the figure illustrates the constituent frequency components of the pulse on the vertical axis and their relative position in time with respect to each other on the horizontal axis. The red line indicates the position of constant phase. The bottom of the figure illustrates the resulting pulse formed by the sum all of the frequencies.
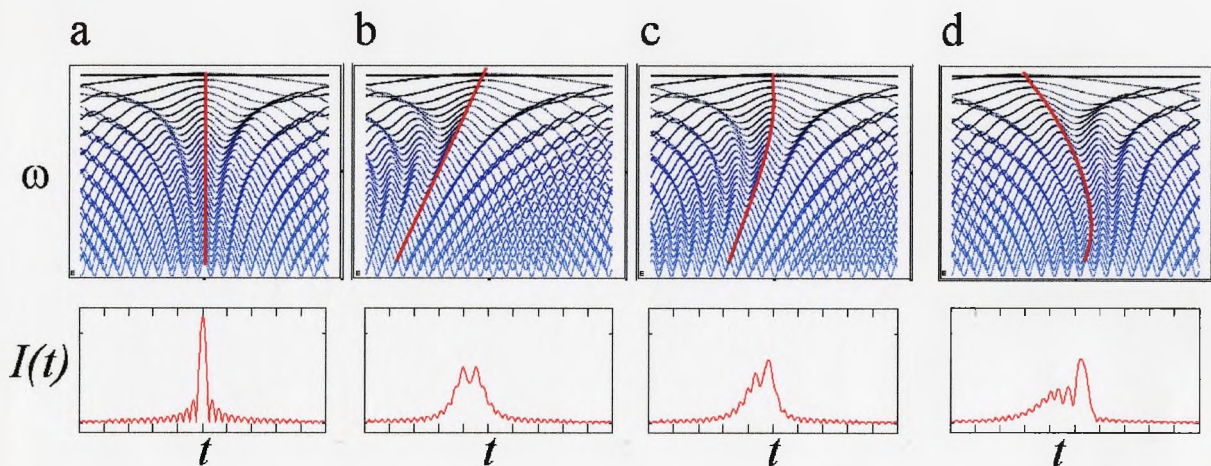
Figure 2.1 Principle of mode-locking: the top plots show the frequency components on the vertical axis and their relative phases on the horizontal axis. The red line indicates the location of constant phase; the bottom plots show intensity profile of the pulse formed by summing all frequencies.

The temporal intensity profile of the pulse depends critically on the relative phase of the constituent frequency components. Figure 2.1a corresponds to perfectly mode-locked laser operation resulting in the shortest, most intense pulse. Figures 2.1b, c and d show examples of a quadratic phase shift or linear frequency shift, cubic phase shift or quadratic frequency shift and higher order phase shift respectively. Clearly the temporal profile suffers despite the fact that in all cases the frequency bandwidth of the pulse is identical.

The electric field of an ultrashort pulse can be described as $E(r,t)$ in the time domain or as $E(r,\omega)$ in the frequency domain. The spatial variables will be omitted in this discussion. Both time and frequency descriptions are equally valid and are related through a Fourier transforms. The choice of domain often depends on the mathematical convenience and the physical phenomenon being investigated. The electric field as a function of time, $E(t)$ and of frequency $E(\omega)$ are related by the following expressions:

$$E(t) = \frac{1}{2\pi}\int_{-\infty}^{\infty} E(\omega)e^{-i\omega t}d\omega \quad \text{and} \quad E(\omega) = \int_{-\infty}^{\infty} E(t)e^{i\omega t}dt .$$

$$2.1$$

2.1.2 Time Domain

The electric field $E(t)$ can be decomposed into the product of a slowly varying envelope $\tilde{E}(t)$ and a phase $e^{-i\phi(t)}$ term such that

$$E(t) = \frac{1}{2}\tilde{E}(t)e^{-i\phi(t)} + c.c , \qquad 2.2$$

where c.c. denotes the complex conjugate. This decomposition is referred to as the slowly varying envelope approximation and is valid only if the spectral bandwidth $\Delta\omega$ is much smaller than the central frequency ω_o; that is $\Delta\omega << \omega_o$. In practice this means that pulses down to ~ 50 fs can be well described by this approximation. The two most often quoted envelope functions are the Gaussian

$$2.3$$

$$\tilde{E}(t) = \tilde{E}_o \exp\left(-\frac{t^2}{\tau_p^2} \right)$$

and the hyperbolic-secant

$$\tilde{E}(t) = \tilde{E}_o \text{sech}\left(\frac{t}{\tau_p}\right),$$ 2.4

where τ_p is the pulse width (i.e. $E(\tau_p) = E_o/e$). In practice, it is more convenient to measure

the full width half maximum FWHM of the pulse (i.e. $E(\tau_G) = E_o/2$). For pulse shapes that

can be described by a Gaussian and a hyperbolic secant function these two quantities are

related by

$$\tau_p = 1.665 \cdot \tau_G \quad \text{and} \quad \tau_p = 1.763 \cdot \tau_S$$ 2.5

The phase function of the pulse in equation 2.2 is given by

$$\phi_{total}(t) = -\omega_o t + \phi(t)$$ 2.6

where ω_o is the carrier angular frequency and $\phi(t)$ is the time dependent phase. The

instantaneous frequency at time t is then given by the first derivative of the total phase

$$\omega(t) = -\frac{d}{dt}\phi_{total}(t) = -\omega_o + \frac{d}{dt}\phi(t)$$ 2.7

If $d\phi(t)/dt \neq 0$ then the carrier frequency varies across the pulse and the pulse is frequency

modulated or chirped (fig 1b,c,d). Phase control is a central part of the ultrafast laser

technology.

The temporal intensity of the pulse is given by

$$I(t) = \frac{1}{2}\varepsilon_o c \left|\tilde{E}(t)\right|^2$$ 2.8

2.1.3 Frequency Domain

In the frequency domain the electric field $E(\omega)$ can be expressed in terms of the envelope function $\tilde{E}(\omega)$ (spectral amplitude) and spectral phase $e^{-i\phi(\omega)}$

$$E(\omega) = \tilde{E}(\omega)e^{i\phi(\omega)}$$
2.9

A Gaussian temporal profile has a Gaussian frequency distribution given by

$$\tilde{E}(\omega) = \tilde{E}_o \exp\left(-\frac{(\omega - \omega_o)^2}{\Delta\omega^2} \right)$$
2.10

where ω_o is the central angular frequency and $\Delta\omega$ is the frequency bandwidth i.e. $E(\omega_o + \Delta\omega)$ = E_o/e. Likewise the derivative of the spectral phase ($d\phi(\omega)/d\omega \neq 0$) describes the phase variation with respect to frequency. This quantity has units of time and represents the delay in the arrival time of a particular frequency component ω relative to the central frequency ω_o. The spectral intensity or simply the spectrum of the pulse is given by

$$S(\omega) = \frac{\varepsilon_o c}{\pi}|E(\omega)|^2 .$$
2.11

2.1.4 Fourier Limit

Since $E(t)$ and $E(\omega)$ are connected by a Fourier transform the pulse width and the frequency bandwidth will have a minimum value of

$$\Delta\omega \cdot \tau_p = C ,$$
2.12

where C is a constant on the order of unity whose exact value depends on the particular pulse shape. The pulse width bandwidth product is the figure of merit in the context of ultrafast pulses. When this limit is reached the time dependent phase is constant ($d\phi(t)/dt = 0$); thus

the instantaneous frequency across the pulse is constant ($\omega(t)=\omega_o$) and the pulse is said to be Fourier or bandwidth limited (fig 1a).

2.1.5 Propagation of the femtosecond pulses

The starting point for all theoretical pulse propagation calculations is the wave equation. In the most general form it can be written as

$$\nabla^2 E - \frac{1}{c^2}\frac{\partial^2 E}{\partial t^2} = -\mu_o\frac{\partial^2 P}{\partial t^2} \qquad 2.13$$

where P is the induced polarization of the material. In general the polarization of the material can be written as

$$P = \varepsilon_o \cdot \{\chi^1 E + \chi^2 E^2 + \chi^3 E^3 \dots\}. \qquad 2.14$$

The first term in the expansion of χ is the linear susceptibility of the medium χ^1 and it is responsible for chromatic dispersion and linear absorption. The second term χ^2 is responsible for second harmonic generation (SHG), sum frequency mixing and nonlinear absorption. However, χ^2 has a non zero value only for materials which lack the inversion symmetry; thus any amorphous substance or symmetric crystals will have $\chi^2 = 0$. Finally χ^3 is responsible for third harmonic generation, four-wave mixing and nonlinear refraction. Higher order terms can be ignored under most circumstances. In the simplest case the polarization is a linear function of the electric field. However, when dealing with ultrafast pulses the nonlinear components of the polarization must be taken into account. The physical reason is that very intense pulses have electric fields on the order of the intrinsic fields holding the material together. Interaction with the laser field will thus modify the properties of that material.

In order to simplify the mathematical treatment several assumptions are often made. First, the response of the material is assumed to be instantaneous. Since many of the processes mentioned above are electronic in origin such an assumption is valid down to about 100 fs. Second, the electric field, polarization and susceptibility are considered scalar quantities. The equation can then be separated into two parts; one which describes the transverse field distribution perpendicular to the propagation direction or spatial mode (x,y), and the other which describes the temporal evolution of the pulse along the propagation direction (z,t). In this case, we are interested in the temporal evolution of the ultrashort pulses in the medium of propagation. The specific details of the derivation can be found in reference [1]. The temporal evolution of the pulses as it passes through a medium is governed by the following equation

$$-i\frac{\partial E}{\partial z} = \beta_1\frac{\partial E}{\partial t} + \frac{1}{2}\beta_2\frac{\partial^2 E}{\partial t^2} + \frac{i}{2}\alpha E + \gamma\,|E|^2\,E\,, \qquad 2.15$$

where E is the slowly varying envelope of the pulse and z is the propagation distance. The first two terms on the right contain the effects of chromatic dispersion. Specifically, the pulse envelope travels with the group velocity $v_g = \beta_1^{-1}$ and the pulse broadening or group velocity dispersion (GVD) is governed by β_2. The coefficients α and γ account for linear absorption and nonlinear properties of the medium respectively. It is common practice to transform equation 2.15 to a frame of reference moving with the group velocity of the pulse $(v_g = \beta_1^{-1})$. Equation 2.15 then simplifies to

$$i\frac{\partial E}{\partial z} = \frac{1}{2}\beta_2\frac{\partial^2 E}{\partial T^2} - \frac{i}{2}\alpha E + \gamma\,|E|^2\,E\,, \qquad 2.16$$

where $T = t - z/v_g$ is time measured in the frame of reference moving with the group velocity of the pulse. This equation is often the starting point for simulating pulse propagation in the optical system or any medium of interest.

2.1.6 Group Velocity Dispersion (GVD)

The effect of material dispersion is one of the most important aspect which has to be considered in and ultrafast applications due to the broadband nature of the pulses. Dispersion leads to pulse broadening and therefore loss of intensity and temporal resolution at the focal point. In order to illustrate the effects of group velocity dispersion, the non-linear term and absorption in equation 2.16 are ignored by setting $\gamma=\alpha=0$. The equation then reduces to

$$i\frac{\partial E}{\partial z} = \frac{1}{2}\beta_2\frac{\partial^2 E}{\partial T^2}, \qquad\qquad 2.17$$

which can be easily solved using the Fourier method. If $E(z,\omega) = FT\{E(z,T)\}$ then in the frequency domain equation 2.17 becomes an ordinary differential equation

$$i\frac{\partial E}{\partial z} = \frac{1}{2}\beta_2\omega^2 E . \qquad\qquad 2.18$$

The solution is given by

$$E(z,\omega) = E(0,\omega)\exp\left(\frac{i}{2}\beta_2\omega^2 z\right), \qquad\qquad 2.19$$

where E(0,ω) is the incident field. A very important feature of this solution is the fact that the envelope of the field is independent of the propagation distance, $|E(z,\omega)|^2 = |E(0,\omega)|^2$.

However, the solution does contain a quadratic spectral phase shift. The solution in the time

domain can be obtained by taking the inverse Fourier transform of equation 2.19, $E(z,T) = FT^{-1}\{E(z,\omega)\}$. In the simple case of a Gaussian pulse in a dispersive medium the equation can be solved analytically. After propagating a distance z in the medium the pulse envelope becomes

$$E(z,T) = \frac{\tau_o}{\sqrt{\tau_p^2 - i\beta_2 z}} \exp\left(-\frac{T^2}{2(\tau_p^2 - i\beta_2 z)} \right),$$ 2.20

where τ_p is the original pulse width. The important feature of the solution, in the time domain, is the fact that the pulse envelope remains Gaussian but the pulse width increases such that

$$\tau(z) = \tau_p^2 - i\beta_2 z = \tau_p \sqrt{1 + (z / L_D)^2}$$ 2.21

while the peak amplitude decreases to:

$$E_z = \frac{\tau_o}{\sqrt{\tau_p^2 - i\beta_2 z}}.$$ 2.22

A convenient length scale defined as

$$L_D = \frac{\tau_p^2}{|\beta_2|}.$$ 2.23

is often used to describe the distance over which the dispersion effects become significant. After traveling a distance of L_D the pulse width increases roughly by a factor of 2. Figure 2.2 illustrates exaggerated effects of GVD on the phase and envelope of an incident Gaussian pulse with an initial pulse width τ_p after propagation in normal ($\beta_2 > 0$) and anomalous ($\beta_2 < 0$) dispersive regions.
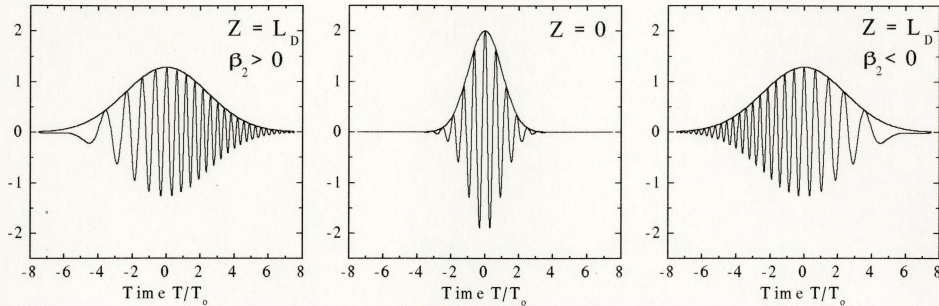
Figure 2.2: Effects of GVD on the phase and envelope of an incident Gaussian pulse after propagating in the normal ($\beta_2 > 0$) and anomalous dispersion region ($\beta_2 < 0$).

In practical terms it is useful to consider the effects of dispersion on the pulse introduced by the optical components within a given setup. For example a setup may contain a 3 mm neutral density filter, a 2 mm $\lambda/2$ plate, and a final focusing objective with 5 mm of glass inside for total of 10 mm of glass. Initial transform limited pulses of 100, 50, 25 and 10 fs would broaden to 100, 51, 32 and 51 fs respectively in 10 mm of BK7 glass. Dispersion management clearly becomes crucial as the initial pulse width approaches tens of femtoseconds.

2.2 Gaussian Beams

Most applications, especially micromachining, require tight focusing of the beams and quantities of major interest are the energy density per unit area or fluence (J/cm^2); and energy per unit area and per unit time or intensity (W/cm^2) in the focal plane. The output of most lasers is well approximated by the Gaussian intensity distribution $I(r)$ which is given by:

$$I(r) = I(0)\exp\left(-\frac{r^2}{w_0^2}\right)$$

2.24

where r is the radial coordinate, $I(0)$ is the on-axis intensity and w_o is the beam waist or point where $I(w_o) = I(0)/e$. The spot size, or beam diameter is then $2w_o$. The on-axis fluence and the intensity of a focused, pulsed laser with a Gaussian beam profile is

$$F(0) = \frac{E_p}{\pi \cdot w_o^2}[\text{J/cm}^2] \quad \text{and} \quad I(0) = \frac{E_p}{\tau_p \pi \cdot w_o^2}[\text{W/cm}^2] \qquad 2.25$$

where E_p is the pulse energy and τ_p it the pulse width (FWHM). In chapters to follow, the spot size, and the fluence and intensity profiles will follow the above definitions.

2.3 The femtosecond laser system

2.3.1 The Tsunami fs oscillator

The heart of our laboratory is the commercial Ti:sapphire amplified laser system from Spectra Physics. The first part of the system consists of a Tsunami oscillator pumped by a neodymium yttrium vanadate (Nd:YVO$_4$) Millennia V, diode-array pumped laser. The Tsunami is a femtosecond oscillator based on a Ti:sapphire crystal as the gain medium. Titanium doped sapphire is the crystal of choice in most femtosecond lasers. This is because sapphire has superior optical quality, thermal properties and a high damage threshold. The Ti:sapphire crystal has an enormous fluorescence bandwidth, which could theoretically support ~3 fs pulses. A typical Ti:sapphire femtosecond laser cavity is shown in figure 2.3.
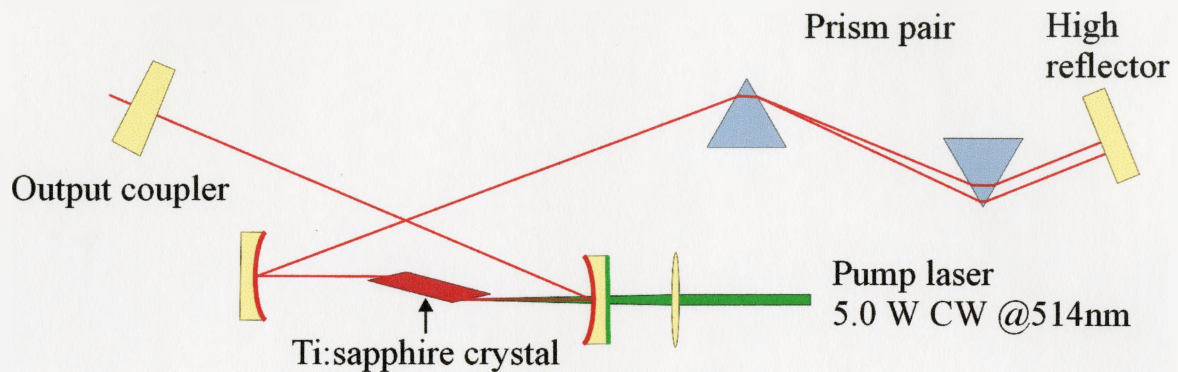
Figure 2.3: Schematic of a typical femtosecond laser oscillator cavity.

The crystal is pumped longitudinally by a argon ion laser at 514 nm or by a frequency doubled $Nd:YVO_4$[1] laser at a wavelength around 532 nm. In normal operation this cavity will lase in a continuous wave (cw) mode with emission centred around the frequency which experiences the highest gain. In order to force the cavity into mode locked operation the oscillating modes must be locked in phase. In Ti:sapphire cavities the crystal itself acts as a mode-locking element relying on Kerr lensing [2,3]. The cavity is aligned to operate in a higher order spatial mode during cw operation and in TEM_{00} during pulsed operation. As the pump power increases, the higher intensity leads to self-focussing in the gain medium and improved overlap of the oscillator modes with the pump beam. Sometimes an extra aperture can be inserted into the cavity to introduce high loss for the cw mode. With an increase in power random fluctuations or mode-beating will then initiate pulsed operation. In order to improve the cavity performance and assure the shortest possible pulses, the positive dispersion in the crystal and other optical components is compensated by an intra-cavity

---

[1] Nd^{3+} is the active atom that can be introduced into a number of host materials, such as YAG, YLF or YVO_4. The emission wavelength is around 1064 nm, and second harmonic around 532 nm. The exact wavelength depends on the choice of host matrix.

prism pair, which introduces effective negative dispersion [4,5]. The Tsunami laser used in our system produces 10 nJ, 80 fs pulses at a repetition rate of 82 MHz.

2.3.2 The Chirped Pulse Amplifier: Spitfire

The second part of the laser system is the Spectra Physics Spitfire ultrafast amplifier seeded by the Tsunami oscillator. The majority of amplifier systems in use today are based on a three stage process called chirped pulse amplification (CPA) [2,6]. Ultrafast pulses cannot be amplified directly since the peak power would quickly reach the damage threshold of refractive optical components, such as Pockels cells, Ti:sapphire crystal and polarizers. Therefore prior to amplification, the laser pulse is stretched to about 200 ps by a grating stretcher, thus reducing the maximum peak power to 10 W. An unstretched pulse of the same energy would reach intensities on the order of 10^{13} W/cm². The stretched pulse is coupled into the amplifier cavity with the aid of a thin film polarizer and a Pockels cell. The s-polarized train of seed pulses is reflected by the polarizer into the cavity. The first Pockels cell is then opened for a very short time (~10 ns) and the polarization of one pulse is rotated by 90 degrees. The amplifier cavity is designed for p-polarized operation and since only the rotated pulse will match this condition the rest will experience high losses. During a single pass through the crystal the pulse energy will only be increased by a factor of 3-4 due to low gain saturation. In order to amplify the pulse by factor of 10^5 the pulse is allowed to circulate in the cavity until all available energy is extracted from the Ti:sapphire crystal.   Once saturation is reached the second Pockels cell is opened rotating the polarization of the amplified pulse by 90 degrees. The rotated pulse is then reflected out of the cavity by the second polarizer (see fig 2.4b). The last step in the process is the recompression of the pulse

to the original duration with the aid of a conjugate grating compressor [7]. The chirped amplification process and a typical amplifier cavity are illustrated in the figure 2.4.

a

Grating pulse stretcher

Solid state amplifier

Grating pulse compressor

Seed pulse from oscillator 100 fs

Stretched pulse 200 ps

Amplified pulse 200 ps

Compressed pulse 120 fs

b

Pockel's cell 1

Thin film polarizer

Pump laser 5 mJ/pulse @ 532 nm

Pockel's cell 2

High reflector

Ti:sapphire crystal

High reflector

Input pulse ⊙

⊙ Output pulse
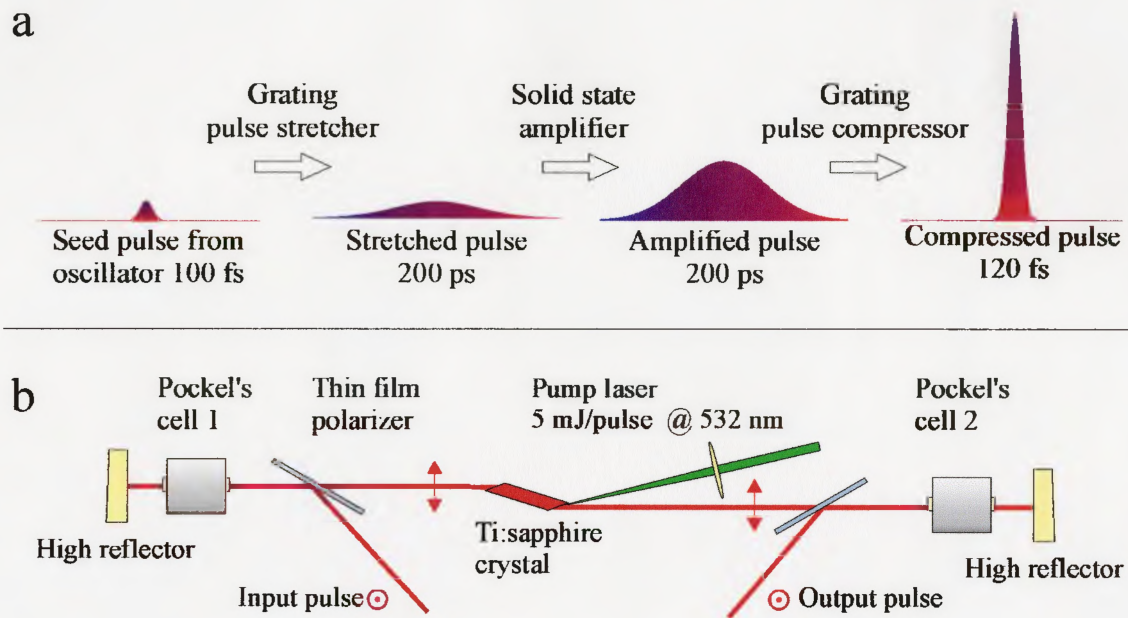
Figure 2.4: a. Principle of chirped pulse amplification (CPA) **b.** Typical regenerative amplifier cavity

Chirped pulse amplification also provides access to pulse durations spanning several orders of magnitude while maintaining all the other laser parameters constant. In our system, fully compressed pulses have pulse widths around 120 fs. By detuning the compressor section the pulse duration can be increased all the way up to 200 ps. If the amplifier is not seeded by a short pulse the lasing action will be initiated by spontaneous emission and without the Pockels cells the laser would operate in a cw mode. However Pockels cells serve as cavity Q-switches and the result is pulsed operation with 10 ns pulses. The laser capabilities of our system are summarized below.

	Tsunami	Spitfire
Pulse width	80 fs	10 ns, 200 ps – 120 fs
Rep. Rate	82 MHz	5 Hz-1 kHz
Maximum pulse energy	10 nJ	0.3 mJ
Central wavelength	790 nm	790 nm

2.4 Femtosecond Diagnostic Tools

2.4.1 Autocorrelators

Measurements of the temporal intensity profiles of laser pulses are usually performed directly with the aid of photodiodes. Direct measurements by electronic devices are limited to the pulses longer than 30 ps. Since femtosecond pulses are three orders of magnitude shorter, the temporal intensity profiles of the pulses must be measured by indirect techniques. Autocorrelation techniques are widely used as ultrashort diagnostic tools. Most autocorrelators are based on the Michelson interferometer design, where the pulse under investigation is split into two replicas by a 50/50 beamsplitter and each replica is send through separate arm. Changing the distance of one arm introduces a time delay τ for the pulse in that arm. The speed of light is used for calibration, that is 0.3 μm path difference = 1 fs delay. The two pulses are then recombined by the same beamsplitter and frequency doubled in a thin nonlinear crystal, most often β-barium borate (BBO). The second harmonic signal intensity will reach a maximum when the two pulses arrive in the crystal at the same time ($\tau = 0$) and the signal will drop to zero when the two pulses do not overlap temporally. Therefore the range of delays over which a second harmonic signal is detected roughly corresponds to the pulse width. More precisely the signal is a convolution

of two replicas of the pulse. The two most common autocorrelator geometries are intensity (non-collinear) and interferometric (collinear). In the intensity autocorrelator the two beams travel parallel to each other and are crossed at shallow angle inside the nonlinear crystal by a lens or mirror. Each pulse produces a second harmonic signal in the crystal. When the two pulses overlap spatially and temporally in the crystal a third beam is generated along the bisector of the two beams (fig. 2.5). The second harmonic signal, generated along the bisector, is measured as a function of the delay. The intensity autocorrelation function can be written as:

$$AC(\tau) = \int_{-\infty}^{\infty} I(t) \cdot I(t - \tau) dt \qquad 2.26$$

The intensity autocorrelation does not provide any information about the phase modulation of the pulse but gives a rough measurement of the temporal intensity profile. In conjunction with spectral measurements, this method can be used to calculate the pulsewidth–bandwidth product. The geometry of an intensity autocorrelator, the beam geometry inside the nonlinear crystal, and a typical trace are shown in figure 2.5.
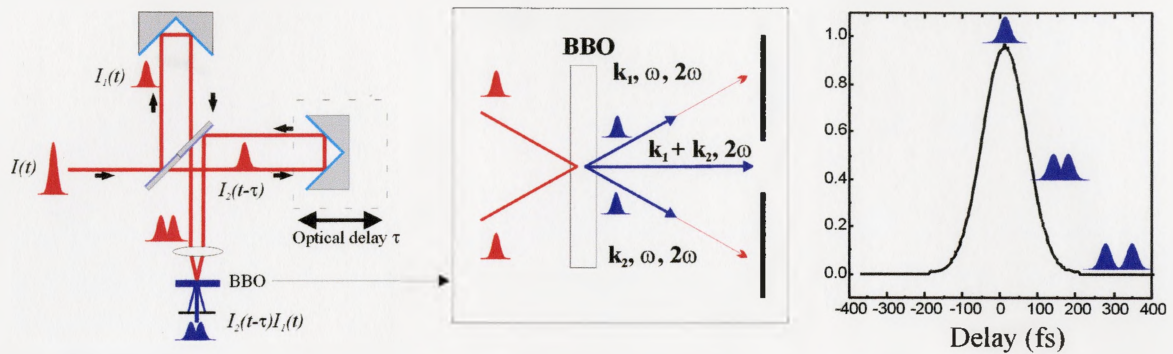
Figure 2.5: (left) Geometry of an intensity autocorrelator, (middle) beam geometry inside the nonlinear crystal, (right) typical autocorrelation trace.

As mentioned earlier, autocorrelation is an indirect measurement method, therefore the pulse shape must be deconvoluted from the measured trace. The autocorrelation half width τ_{AC} is always greater then the actual pulse width τ_p by a factor which depends on the shapes of the pulses. For Gaussian and hyperbolic secant intensity profiles the proportionality factors are 1.414 and 1.545 respectively.

In the interferometric autocorrelator the two beams are recombined collinearly. The geometry of an interferometric autocorrelator is shown in the figure 2.6 along with first and second order autocorrelation traces. Varying the length of the delay arm results in an interference pattern, which can be described as:

$$AC(\tau) = \int_{-\infty}^{\infty} |(E(t) + E(t - \tau)|^2 dt \qquad 2.27$$

First order autocorrelation (fig. 2.6) is related to the coherence time of the radiation, thus it is not unique to short pulses. In fact white light will have a very narrow autocorrelation trace due to low coherence. The Fourier transform of the first order autocorrelation is the spectrum of the light. In fact this is the principle of the Fourier transform spectrometer.

Second order autocorrelation can be obtained by frequency doubling the output of the interferometer in a nonlinear crystal. The second order interferometric autocorrelation function can be written as:

$$AC(\tau) = \int_{-\infty}^{\infty} \left| \left| (E(t) + E(t-\tau) \right|^2 \right|^2 dt \qquad 2.28$$

The second order autocorrelation can be used to measure the pulse duration and presence of phase modulation. Typical second order autocorrelation trace is shown on the right side of figure 2.6.
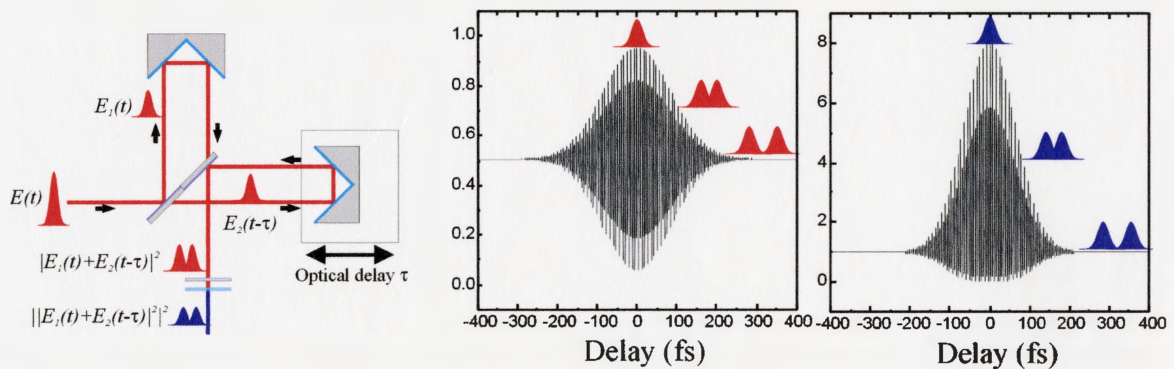
Figure 2.6: (left) Geometry of an intensity autocorrelator, (middle) 1st order autocorrelation trace, (right) 2nd order autocorrelation trace.

There are also a number of more advanced techniques, which can be used to fully characterize pulse shape and relative phase of constituent frequency components. Most of these techniques are based on frequency resolved optical gating in conjunction with phase retrieval algorithms. Discussion of these techniques is beyond the scope of this thesis and the interested reader is referred to [2] and references there in.

2.4.2 Spectrometer

To the first order approximation, the pulse quality can be calculated by measuring the pulsewidth-bandwidth product ($\tau_p \cdot \Delta\omega$). By the same token, the minimum pulse duration can be estimated based on the bandwidth of the laser. Spectral measurements of a femtosecond pulse do not require any specialized equipment and a standard scanning or array spectrometer can be used. In our laser system the spectrum, of the laser is monitored with the Ocean Optics spectrometer. The Ocean Optics is an integrated grating spectrometer with a linear CCD detector. The resolution of the device is roughly 0.5 nm and covers the spectral range from 1100 to 500 nm.

2.4.3 Beam Profile Measurements

Measurements of the beam waist ($2w_o$) at the focal point of the focusing objective were measured by the scanning knife edge technique. In this method a sharp edge is slowly moved across the beam profile and the total transmitted intensity is recorded by a large area photodetector as a function of the knife position X. The measured signal is a convolution of the beam profile $U(x)$ and a step function $\Phi(x\text{-}X)$ (knife-edge)

$$S(X) = \int_{-\infty}^{\infty} U(x) \cdot \Phi(x - X)dx .$$

2.29

Figure 2.7 illustrates the schematic implementation of this method and a typical scan profile.
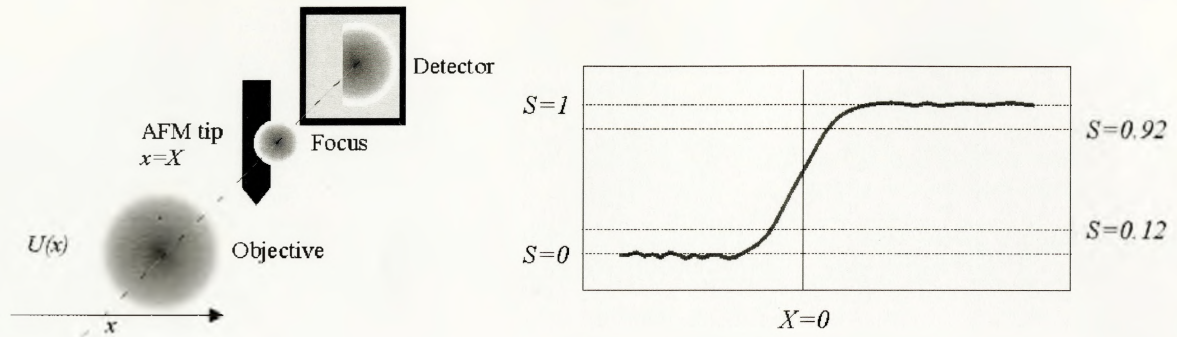
Figure 2.7: Principle of scanning knife edge spot size measurements.

The spot size $(2w_o)$ at the focus of the objective can be read directly from the scan profile. The distance between $S = 0.92$ and $S = 0.12$ corresponds to the spot size for a Gaussian intensity profile. The measurement of spot sizes ~ 10 μm requires an extremely thin knife edge and a high resolution translation stage. In our setup we use an AFM (atomic force microscope) cantilever as the knife edge and a computer controlled motorized-micrometer driven translation stage with minimum step size of 0.1 μm.

Chapter 3

X-ray Emission from Femtosecond Laser Micromachining

Prior to initiating our laser micromachining work we set out to investigate radiation emitted during the femtosecond laser ablation process. In this chapter I will describe experiments and results of our investigations of radiation in the 4 keV to 25 keV range produced under typical micromachining conditions. The results presented in this chapter were presented during the Conference for Lasers and Electro-Optics (CLEO 2000) and submitted to the journal Applied Physics A.

3.1 Introduction

The availability of high peak power femtosecond laser systems has opened a new era in plasma physics research [8,9]. Focussing high energy femtosecond pulses to a spot size near the diffraction limit onto a solid target leads to generation of very hot plasmas at near solid state density. The photon emission from ultrafast laser generated plasmas is emitted in picosecond bursts [10,11] and can span an energy scale from vacuum ultraviolet (VUV), soft x-ray [12], to hard x-ray [13] up to MeV photons [14] depending on the excitation fluence. The ability to generate such extreme wavelengths with a table-top system along with the

unique characteristics of the emission has opened interesting possibilities for fundamental and applied research. The short temporal duration of the pulses has been exploited to study time resolved dynamics of chemical reactions [15], transient x-ray absorption spectroscopy [16], ultrafast lattice dynamics [17,18] and biological imaging [19]. Currently the development and use of femtosecond lasers as an ultrafast x-rays source is an area of intense research. Lasers deployed in these fields have typical pulse energies on the order of 1 mJ-1 J/pulse and low repetition rates around 10 Hz. Focusing 1 J, femtosecond pulses close to diffraction limit leads to intensities exceeding 10^{19} W/cm^2 [20]. Often the compressor stage and beam delivery optics are enclosed in modest size vacuum chambers to avoid the non-linear effects in air. On the other hand, commercial femtosecond laser systems available for industrial and scientific research are typically much smaller with pulse energies between 1 µJ-1 mJ and operate between 1 kHz and 250 kHz and pulse widths down to ~ 20 fs. If such pulses are focused close to the diffraction limit intensities on target can reach ~ 10^{17} W/cm^2. With continuous technological advances such systems are quickly becoming common features of many scientific laboratories. During the past decade the use of femtosecond lasers in laser machining and material processing has also attracted significant attention. Micromachining with ultrafast pulses has been shown to yield superior results compared to lasers of longer pulse duration, especially well established nanosecond laser technology [21,22]. Also, the first kHz, mJ femtosecond micromachining workstation has already appeared on the market (produced by Clark-MXR). Despite the trend in using femtosecond lasers as materials processing tools the hard radiation resulting from interaction of the laser pulses with the machined materials has not been characterized in this context. In

a number of preliminary experiments, we investigated and characterized radiation spectra and absolute dose rates produced under typical laser micromachining conditions.

3.2 Experimental Setup and Experiments

The laser system used in these experiments was discussed in detail in chapter 2. Briefly, the amplifier delivers 800 nm pulses of 120 fs duration, with up to 0.3 mJ at a 1 kHz repetition rate. Two different experimental setups illustrated in figure 3.1 were used.
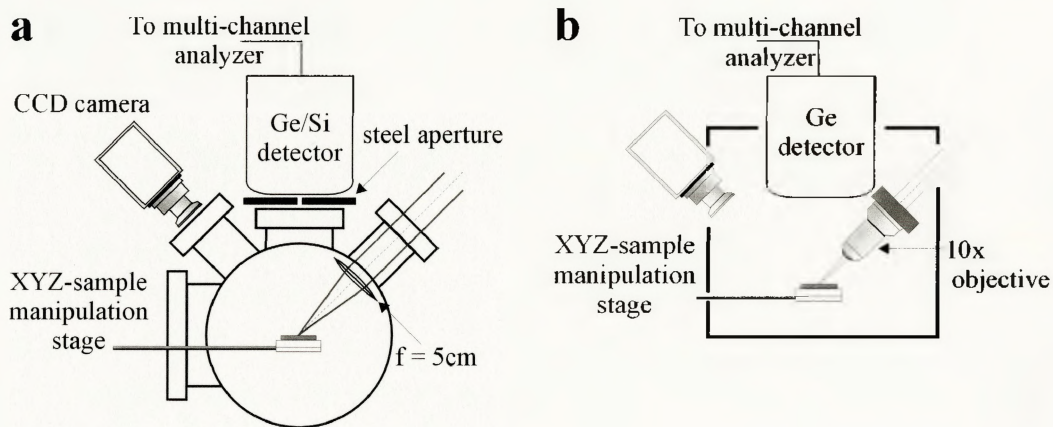
Figure 3.1: a. Experimental setup used to study x-ray produced by high energy pulses, **b.** Experimental setup to study x-ray production under real micromachining conditions.

Figure 3.1a illustrates the setup used to study and characterize radiation produced by relatively high energy pulses ~0.3 mJ/pulse. The p-polarized laser pulses were focussed on the target by f = 5 cm plano-convex lens (uncoated). The spot-size of the lens was measured by the scanning knife edge technique (see chapter 2) to be 15 μm. The target was manipulated by a computer controlled xyz translation stage with a maximum translation speed of 200 μm/sec inside a 5 mm thick-walled stainless steel chamber at ambient pressure. The sample condition was monitored by a CCD camera through one of the view ports. The

x-ray spectra were acquired with the two different detectors. The first comprised a 25.3 mm diameter, 20 mm thick Germanium detector (Canberra Industries 2020R) shielded by 0.5 mm beryllium window and cooled by liquid nitrogen (LN2). Signal processing was performed by a charge sensitive preamplifier and a multi-channel analyzer system (Series 5000 MCA by Aptec Nuclear Inc.) with a 4 μsec pulse shaping time. The resolution of this system was 400 eV (FWHM) as quoted by the manufacturer. The second detector used was a 16 mm diameter, 5.8 mm thick lithium drifted silicon detector (Ortec SLP 16220-S by EG&G) shielded by a 0.50 mm thick beryllium window and cooled by LN2. The signal processing was performed with a pulsed optical feedback preamplifier and DSA2000 digital spectrometer using Genie 2K software (Canberra Industries). The resolution of this detector was 220 eV (FWHM). However, the actual resolution observed in our measurements was lower by a factor of two. The reduction in resolution was attributed to the RF pickup produced by our laser system. Both of these detectors are designed for low peak intensity x-ray sources, however x-rays produced by femtosecond lasers are emitted in bursts on the order of several picoseconds, orders of magnitude shorter then the 4 μs pulse shaping time of the detectors. Therefore if special care is not taken acquired spectra will feature artefacts, such as pile-up. Pileup occurs if multiple x-rays of the same energy are absorbed within the pulse shaping time of the detector. Their energies are then summed and interpreted as a single x-ray photon. Figure 3.2 clearly illustrates the pileup effect with ghost peaks appearing at integer multiple values of the main peak.
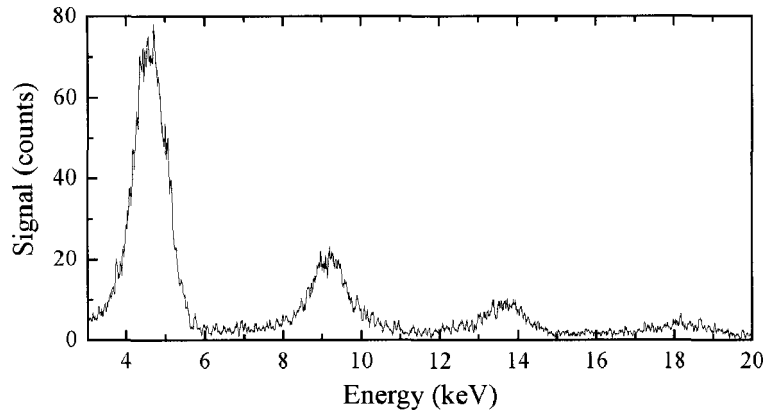
Figure 3.2: Ti x-ray spectrum illustrating effects of pileup

This problem cannot be completely eliminated without going to a diffractive spectrometer. In order to minimize this effect in our measurements a 1 mm stainless steel plate with 1 1 mm aperture was inserted in front of the detector in order to reduce the average x-ray detection rate to approximately 1 event per 10 laser pulses. Also the translation stage speed was adjusted to keep the count rate constant. Both spectrometers were calibrated with the aid of multi-energy radiation source. In addition to the two spectrometers a thin windowed ionization monitor (Bicron RSO-5) designed for soft x-ray measurements (cut-off ~ 8 keV) was used to measure the absolute x-ray doses produced. In the first setup all detectors were placed 13 cm from the target. The second setup illustrated in the figure 3.1b was used to study x-ray emission under actual micromachining conditions. Here the p-polarized beam was focussed on various targets at normal incidence by a 10x microscope objective. The spot-size at the focus of the microscope was measured to be 9 μm. The spectra were obtained via the germanium detector positioned ~ 5 cm from the target at 45°. The steel aperture was not used in these experiments since the total x-ray yield was significantly lower.

Targets used in these investigations included a number of pure metals and semiconductors, such as: Al, Ti, Cr, Fe, Cu, Zn, Ge, Nb, Mo and W. None of the samples were given any special treatment prior to laser irradiation. The Cu sample used was a CO_2 laser mirror and therefore had a high surface quality. Therefore the Cu target was used for most of the studies involving the intensity dependence of x-ray emission.

3.3 Experiments and Results

In the first series of experiments, the setup depicted in figure 3.1a was used to irradiate the targets with relatively high pulse energies ~0.3 mJ/pulse, which corresponds to the intensities on target of $2 \cdot 10^{15}$ W/cm². Figure 3.3 shows the x-ray spectrum of Cu obtained with the silicon detector. The spectrum is corrected for air attenuation and detector response.
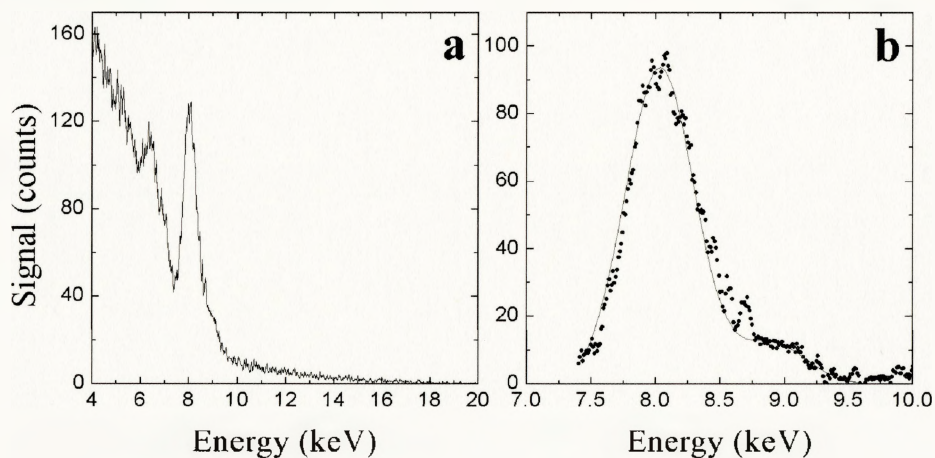
Figure 3.3: a. Corrected Cu spectrum. **b.** K_α and K_β lines

The spectrum consists of 8.0 keV K_α (1.54 Å) and 8.9 keV K_β (1.39 Å) Cu emission lines radiation with the expected 7:1 ratio (fig 3.3b) superimposed on continuum bremsstrahlung

background. The background spectrum stretches all the way up to ~25 keV. The weak

background can be approximated by the Planck spectral distribution function ρ(υ) of a black-

body source at 9.8 MK (0.84 keV)

$$\rho(\upsilon) = \left(\frac{8\pi h \upsilon^3}{c^3} \right) \left(e^{h\upsilon/kT} - 1 \right)^{-1} ,$$

where c is the speed of light, h is Planck constant and υ is the frequency of the emitted

radiation, k is Boltzmann's constant and T is the plasma temperature. The fitted curve is

shown in figure 3.4 on linear (a) and logarithmic (b) scales.
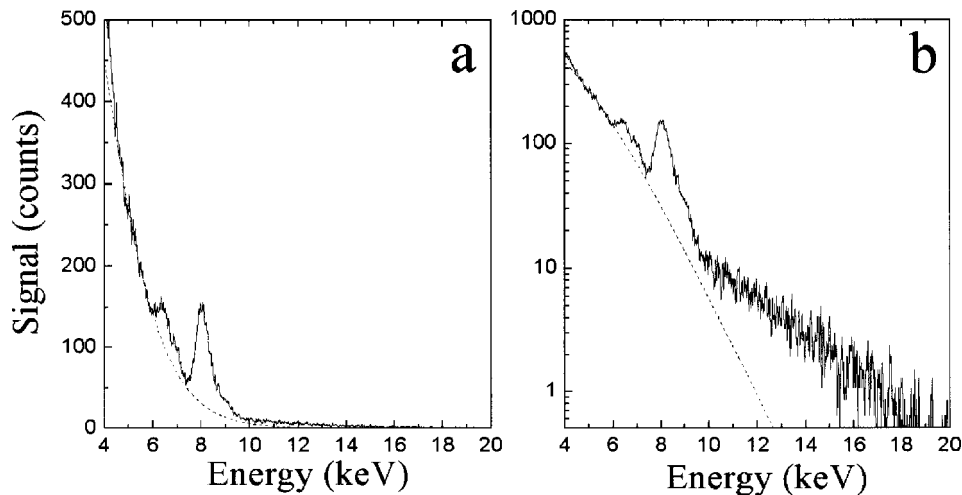
Figure 3.4 a. Blackbody at 9.8 MK fit to the radiation distribution, **b.** Same plot shown on a logarithmic scale.

The deviation from the Planck function at the lower end can be attributed to large uncertainty

in the correction factors (air attenuation and the detector efficiency below ~5 keV). The

same graph plotted on the logarithmic scale (fig 3.4 b) also reveals a much slower falloff on

the higher energy end (>10 keV). This behaviour is attributed to the superthermal electrons

in the plasma. In order to convince ourselves that this spectral feature was not an detector

artefact caused by pile-up effect we have inserted 1 mm glass slide in front of the aperture

and repeated the run. The glass slide strongly attenuates radiation below 10 keV while transmitting higher energy x-rays almost untenanted. The observed spectrum shown in fig. 3.5 has the same high energy tail as observed above thus illustrating that the effect is real.
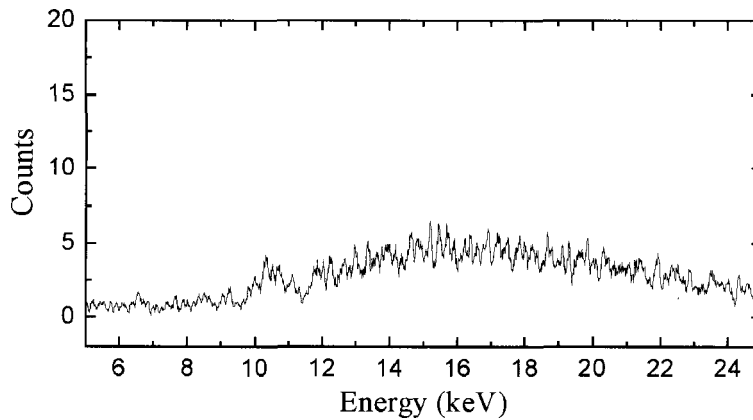
Figure 3.5: X-ray spectrum transmission spectrum through 1 mm glass slide.

In the next set of experiments we have acquired x-ray emission spectra of Al, Cr, Fe, Cu, Zn, Ge, Nb, Mo and W excited by laser intensities of $2.0 \cdot 10^{15}$ W/cm². The spectra were collected with the Germanium detectors using the setup depicted in figure 3.1a. The spectra obtained are shown in the figure.
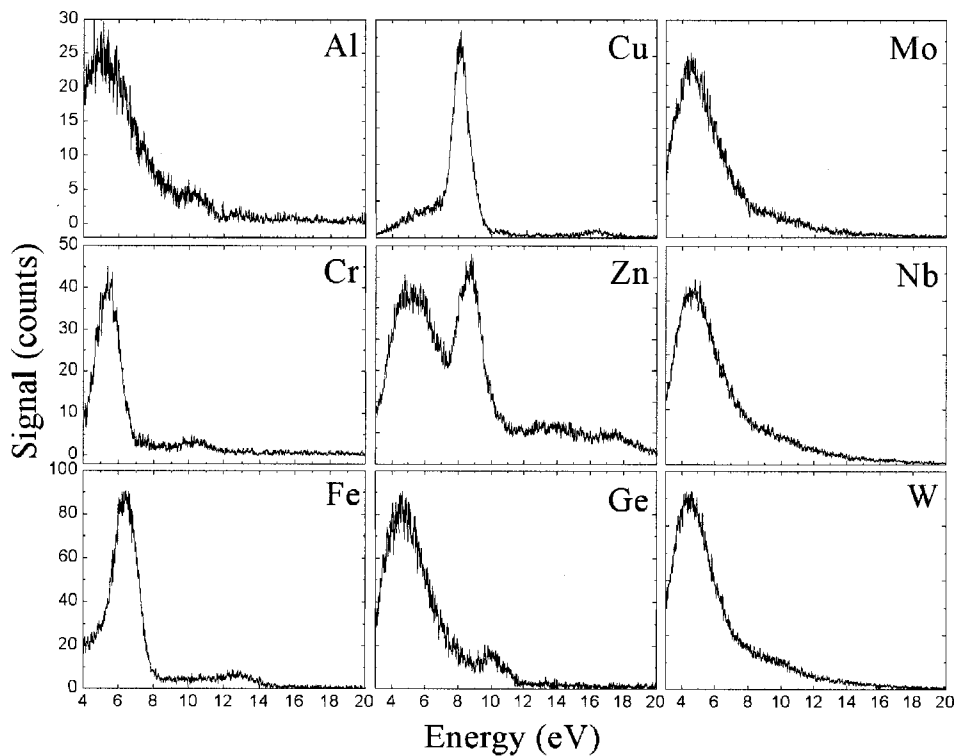
Figure 3.6: The x-ray spectra of Al, Cr, Fe, Cu, Zn, Ge, Nb, Mo and W excited by laser intensities of 2.0· 10^{15} W/cm².

The spectra of elements with Z<32 show K line emission superimposed on a continuum bremsstrahlung background while elements with Z>32 show only the bremsstrahlung emission. Note that the K line of Al and the L and M lines of the other materials fall outside the energy region of our detector. Furthermore, Ti, Cr, Fe and Cu show predominantly only K line emission. This illustrates that femtosecond laser x-ray sources can produce very clean, pulsed spectral emission. Additional filtering can further be used to clean up the spectrum.

In the next series of experiments, we concentrated on measuring the relationship between line and continuum radiation as a function of pulse intensity. Starting with the Cu target, the pulse intensity was decreased by attenuating the laser beam until only a continuum

background was observed. At this point, the Cu target was replaced by Fe whose K line lies

at 6.4 keV. Once again both the line emission and the background was observed. The laser

intensity was then reduced further until the line emission disappeared and the target was

changed to Ti and K line emission was observed once again. Along with the results

discussed above this clearly illustrates the threshold nature of the radiation emission

depending on the Z value of the target. Thus as soon as the high energy end of the Planck's

emission exceeds the threshold energy, a K emission line appears in the spectrum.

In order to quantify the dose rate of x-ray radiation emitted from the Cu target the

Germanium detector shown in figure 3.1a was replaced by the ionization detector (RSO-5).

The dose rates were measured under the same laser conditions as in the spectrum

measurements. Maximum dose rates on the order of ~10 mSv/hr (~1 rem/hr) were measured

13 cm in front of the target when the target was translated at 150 μm/s. The detector used

has a low energy cut-off around 8 keV with sensitivity dropping to 25% at 8 keV (according

to the company). Based on the spectral radiation distribution and assuming isotropic emission

we estimate the total x-ray photon yield of ~10^5 per laser pulse (10^{15} IR photons) or ~10^8

photon/s into the forward hemisphere. Based on these estimates the x-ray conversion

efficiency in the 5-20 keV range is 10^{-8} %. The x-ray yield below 8 keV increases as $I^{2.8+/-0.3}$

between 0.1 and 0.3 mJ/pulse (7· 10^{14} and 2· 10^{15} W/cm^2), indicating that higher x-ray yields

can be obtained by increasing the excitation pulse intensity. A similar intensity dependence

of hard x-ray yield, in the energy range of >50 keV was reported by M. Schnürer et al. [13]

with laser intensities between 5· 10^{16} and 5· 10^{17} W/cm^2.

The emitted x-ray flux also depends critically on the focusing conditions and on the target speed. A decrease of the x-ray yield with decreasing feed rate or in the case of irradiation of stationary targets can be attributed to the rapid material removal from the irradiated area and to the shadowing effects of the trenches or holes.

The setup depicted in figure 3.1b was used to investigate the radiation emitted the near plasma formation threshold. The copper sample was hit at normal incidence with pulse energies from 9 to 1 μJ. The germanium detector was placed 5 cm from the target and emission was collected at 45°. Figure 3.7 shows Cu x-ray spectra excited by 8.4 μJ, 2.7 μJ and 2.0 μJ pulses.
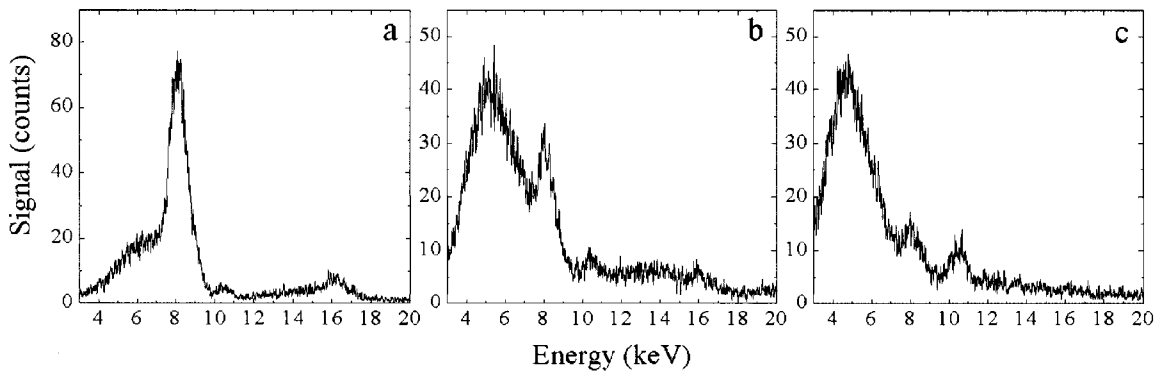
Figure 3.7: Cu x-ray spectra excited by (a) 8.4 μJ, (b) 2.7 μJ and (c) 2.0 μJ pulses

Once again the dependence of line emission on the pulse energy can be clearly seen. At a pulse energy of 8.4 μJ continuum and line emission are present. A reduction of the pulse energy leads to a drop in a total yield and diminished line emission.

3.4 Discussion

3.4.1 Workplace Environment

The nonlinear dependence of the total x-ray yield on the laser intensity implies that the generation of hard radiation must be taken into consideration when designing femtosecond laser based processing workstations. We have shown that maximum dose rates of ~10 mSv/h were detected during micromachining of metals with modest pulse energies 13 cm away from the source with the majority of the radiation emitted below 10 keV. To put these numbers in perspective, we note that the average annual effective dose equivalent due to background radiation is ~ 3 mSv/year. Background radiation includes highly penetrating cosmic radiation and other natural sources, as well as radon radiation, which is mainly affects the lungs. Therefore the value quoted refers to absorption by the entire body. Soft x-rays below 10 keV generated during laser micromachining are absorbed mostly by the skin and eyes. The mass attenuation coefficient for 10 keV in skin is 5.37 cm^2g^{-1}, therefore the bulk of the x-rays produced under the conditions pertaining to our experiments only penetrate 2 mm (1/e) into the body. According to the International Commission on Radiation Protection (ICRP) the annual limits are 20 mSv for occupational situations and 1 mSv for public exposure. That corresponds to an equivalent annual dose limit of 150 mSv and 15 mSv to the lens of the eyes and 500 mSv and 50 mSv for skin, hands and feet for occupational workers and the public respectively. Thus persons working with femtosecond machining systems on a regular basis may exceed maximum the recommended doses if appropriate precautions are not taken. Furthermore our 0.3 mJ pulse energies were rather modest compared to typical 1

mJ systems sold for micromachining purposes. The $I^{2.8}$ dependence suggests that much higher dose rates could be reached. In addition to increased dose rates, the x-ray spectrum may also shift to the higher energy x-rays. X-ray energies in the range of 20 keV penetrate further into the body (up to 12 mm 1/e at 20 keV) and absorption by internal organs may begin to become possible. However knowing the spectral features and the emitted doses it is very easy to shield against the radiation. For example 10 keV and 50 keV x-rays will be attenuated by a factor of 10^9 and 1.3 respectively in 3 mm of Al, and by a factor of 10^{177} and 10^2 in 3 mm of steel. In addition to shielding, increasing distance to the work area will decrease the average field by $1/r^2$ since laser plasma is essentially a point source.

3.4.2 Micromachining

Focussing the laser beam to the diffraction limit means that the confocal parameter (Rayleigh range) is on the order of a micron. Since the total x-ray yield critically depends on the focussing conditions due to high nonlinearity, a simple monitoring detector can be used as a very sensitive feedback signal in a closed loop focussing system. Tight focussing is especially critical in the machining of complex, non-planar surfaces. At the same time x-ray detectors could serve as a monitoring system if the material being processed consists of different elements. X-ray spectroscopy is a more convenient diagnostic tool than optical spectroscopy since only a single emission line is needed to identify a given element. Plasma emission in the optical region exhibits a large number of lines, which lie mostly in the vacuum ultraviolet region (VUV) making fast identification of constituents difficult. X-ray measurements can also be performed in ambient atmosphere whereas optical spectroscopy requires a vacuum spectrometer.

3.4.3 Laser based x-ray sources

Although our work was aimed at the study of x-ray generation during femtosecond laser machining, our results also suggest that a modest size femtosecond laser system can be used as a bright, tuneable x-ray source. Although conversion efficiencies per excitation pulse in our experiments were rather low, several modifications can increase the total x-ray yield. We have observed an increase in the x-ray production with increasing the target speed. During laser machining roughly 1% of the pristine surface was moved into the focus area. Scanning the target fast enough to ensure a pristine surface for every laser shot (> 1 mm/sec) would greatly increase the x-ray yield. Several authors have also shown that the use of structured surfaces [23] and use of a weak prepulses [24] can further increase the total yield. High repetition systems may also improve the signal to noise ratio by making various counting and averaging experiments much more practical. A true advantage of laser-produced x-rays over conventional sources is the ultrashort pulsed duration, which allows the study of dynamic events on a very short time scale. A number of groups have already used the x-ray pump-probe techniques to study melting and ablation of semiconductors [17,18]. However, in those cases high power, low repetition rate lasers are being used as sources.

Soft x-rays produced by laser based x-ray sources can also be used in imaging applications. Changing target material allows easy wavelength tuning for applications such as differential absorption imaging demonstrated by Tillman *et al.* [19]. Currently synchrotron sources are still used for similar applications. Imaging applications would also benefit from high repetition rate lasers since exposure times can be decreased significantly by moving from 10 Hz to 1 kHz. Figure 3.8 shows a x-ray image of a microchip developed by

a laser based x-ray source. The image below was taken using a Polaroid film placed inside a thin aluminium foil shielding and irradiated by a 0.6 mJ laser based source operating at 1 kHz.
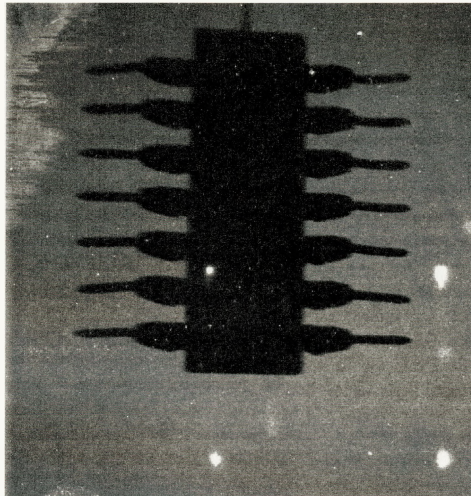
Figure 3.8: Polaroid x-ray picture of a microchip developed by laser based x-ray source. **Courtesy of Jan Thøgersen from Århus University.**

3.5 Summary

The main goal of our experiments was to investigate the spectral nature and absolute dose rates of x-rays emitted during femtosecond laser micromachining. We have shown that relatively low energy pulses (~0.3 mJ) can excite x-rays with the high energy tail extending up to 25 keV. The majority of the radiation was emitted below 10 keV with the radiation distribution approximated by a blackbody source at 8.9 MK (0.89 keV). Under our experimental conditions K line emission was observed from materials with Z<32. The emission exhibited threshold like dependence on the intensity. We have also measured the total x-ray dose rates during laser machining of various targets and observed dose rates on

the order of 10 mSv/h. Our work also illustrates interesting possibilities for using modest

size, high repetition rate systems as pulsed x-ray sources for spectroscopic and imaging

applications.

Chapter 4

Femtosecond Ablation of Semiconductors

4.1 Introduction

Recently, research in the area of femtosecond laser ablation of solids has received a great deal of attention due to the considerable potential in the areas of micromachining and material modification [25,26]. Advances in femtosecond laser technology during the past decade promise to introduce ultrafast systems to the industrial market. All solid-state, amplified laser systems based on the Ti:sapphire crystal have become more common, cheaper, robust and much easier to use. The use of femtosecond pulses offers very interesting possibilities for material processing, especially on the micron scale due to the unique properties of ultrafast pulses. The damage threshold of materials has been shown to decrease with decreasing pulse duration [27,28] since very high peak intensities can be achieved with relatively low pulse energies. For instance, focussing a 100 fs, 1 mJ pulse to a spot size of 10 μm leads to intensities on the order of 10^{15} W/cm^2. In order to obtain the same intensity with a 10 ns laser, the pulse energy would have to be 100 J. A short

interaction time with the target leads to reduction of the lateral damage and thermally induced material stress [29]. Furthermore, the energy absorption and eventual material removal are separated temporally and the trailing edge of the laser pulse does not interact with the expelled material. Absence of plasma shielding allows very strong material excitation prior to material removal. Extreme intensities, easily attainable by focusing ultrashort pulses, lead to a wealth of nonlinear processes, which can be harnessed in a variety of micromachining applications. For example, femtosecond lasers can be used for precise machining of materials which are difficult to process mechanically or with conventional lasers, such as dielectrics [26], ceramics [30], polymers [31], biological hard tissue [32,33], corneal tissue [34], as well as metals and semiconductors [35,36]. It is also possible to produce features beyond the diffraction limit by reducing the pulse energy to the point where only the central part of the beam profile exceeds the material damage threshold [36,37] or by using near field techniques [38]. In the case of materials which are normally transparent in near infrared, it is possible to machine features in the bulk material, without damaging the entrance or exit surfaces [39]. A number of groups have demonstrated the possibility of using this technique for the direct writing of waveguides and gratings in dielectrics [40], recording 3D optical storage media [41, 42] and production of long period fibre gratings [43]. Femtosecond laser ablation and micromachining of materials is an area of intense research, which offers plenty of room to explore fundamental aspects of laser-matter interaction, as well as explore practical issues associated with direct writing, drilling and material modification.

Laser processing of semiconductors has been one of the areas of intense fundamental [44] and applied research [45,46] for a long time due to the technological importance of semiconductors. A large body of work is available on this topic; however, the literature covers mostly cw and short-pulse nanosecond laser processing [45, 47]. More recently the study of ablation and micromachining of semiconductors has been extended to femtosecond pulse durations. The dynamics of single shot ablation of semiconductors were studied by number of techniques including optical pump-probe [48, 49], time of flight mass spectroscopy [50, 51] time resolved microscopy [52], and temporally resolved x-ray diffraction [53, 54]. Many theoretical models have also been proposed to model ultrafast heating [29, 55, 56] and ablation processes [57, 58]. However, to our knowledge, detailed systematic studies of the material properties, particularly surface morphology, structural and compositional changes resulting from single shot femtosecond laser ablation have not been reported. In our experiments we have concentrated on detailed studies of the aftermath of the laser ablation of three technologically relevant semiconductors: Si, GaAs and InP. In particular we have examined the effects of the ablation process on the material structure and composition as well as measured ablation rates and damage thresholds. Our experimental conditions were similar to those reported in refs. 49-52 and provide a supplement to the study of ablation dynamics. Analytical tools used to study the material properties were scanning electron microscope (SEM), atomic force microscope (AFM), transmission electron microscope (TEM) and energy dispersion x-ray spectroscopy (EDX).

4.2 Experimental Setup

The laser system used in this work was discussed in chapter 2. Our micromachining setup is shown in Figure 4.1.
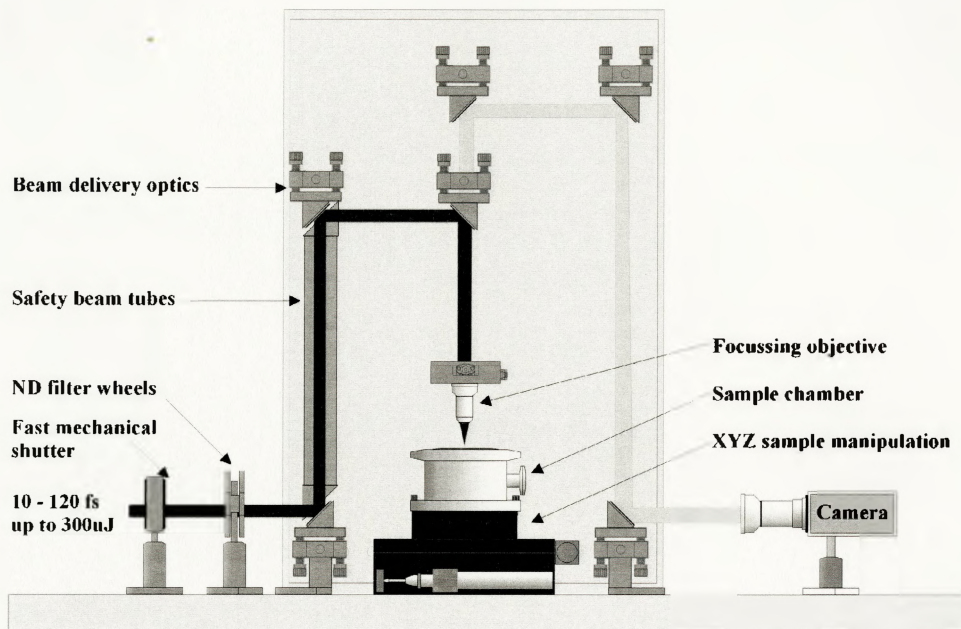
Figure 4.1 Femtosecond laser micromachining setup

The output from the amplifier was delivered to the setup by several dielectric mirrors. The energy of the laser was adjusted with a set of thin (1 mm) reflective neutral density (ND) filters in steps of 0.1 OD (OD = $\log(I_0/I)$). The laser was focused on the sample by a 10x microscope objective (Newport M-10x). The spot size ($2w_0$) of 7 μm at the focus was measured by a scanning knife edge technique which was discussed in chapter 2. A fast mechanical shutter, synchronized with the laser, was used to control the number of pulses delivered to the sample. A confocal imaging system and a CCD camera were used to

monitor the machining process on-line. Semiconductor samples were placed inside a small vacuum chamber mounted on a computer controlled xyz translation stage with maximum linear speed of 200 µm/s and the minimum step size of 0.5 µm. The laser beam was delivered through a thin, uncoated sapphire window (200 µm) cut perpendicular to the c-axis to avoid birefringence effects in the window.

4.3 Single Shot Measurements

The starting point of our investigations included analysis of the material after irradiation with single fs laser pulses. The samples of [100] Si, GaAs and InP were placed in the sample chamber under rough vacuum (100 mTorr) and hit with pulse energies ranging from 1.8 µJ to 10 nJ. The ablation experiments were always performed under conditions of a spatially Gaussian laser pulse. The fluence and intensities quoted in the subsequent discussion refer to the central part of the beam profile. The sample chamber was translated between each shot to ensure a pristine surface for every laser shot.

Changes in surface morphology and size of the ablated features were characterized by means of scanning electron microscope (SEM). The depth and crater profiles were measured with the aid of atomic force microscope (AFM) in the contact mode. Crystal structure and composition in the vicinity of the ablation sites were investigated with a transmission electron microscope (TEM) equipped with an energy dispersive x-ray spectrometer (EDX) and an electron energy loss spectrometer (EELS). The TEM samples were investigated in plan view having been prepared by standard techniques of mechanical back thinning followed by argon ion beam milling.

4.4 Results

In all our ablation experiments no abrupt changes in the surface morphology were observed with increasing pulse energy. However, three ablation regimes can be identified based on the observed surface morphology and characteristic debris patterns. The details of the three regimes vary somewhat between Si, GaAs and InP and will be discussed in detail later. General comments, which apply to all three materials, will be presented first.

The first ablation regime observed was the near damage threshold regime, corresponding to pulse energies of tens of nJ, corresponding to the energy fluence below 100 mJ/cm^2. The damage threshold of the material was taken as the pulse energy above which visible surface modification was observed under SEM. At the material damage threshold features on the order of 500 nm were observed. The surface morphology was indicative of melting followed by resolidification with minimum loss of material. With an increase of the pulse energy the size of the damaged area increased and formation of craters with a distinct rim at the outer edge was observed. In the first ablation regime the ablated areas were typically less then 2 μm in diameter and less than 50 nm deep. Figure 4.2 shows SEM images and corresponding AFM profiles of the ablation features in the near damage threshold regime.

Figure 4.2 SEM images (top) and corresponding AFM profiles of ablation craters in the near damage threshold regime. The blue line indicates the position of the surface prior to irradiation; the red curve shows the Gaussian laser beam profile on the sample surface.

The blue line indicates the surface position prior to irradiation. The red curve shows the Gaussian laser beam profile on the sample surface. In all cases, near the damage threshold the affected areas were much smaller then the spot size ($2w_o$ = 7 μm), indicating the high nonlinearity of the process, where only the intensity over the central part of the beam exceeds the damage threshold. TEM analysis of the areas immediately outside of the craters showed no evidence of structural or surface damage. The high nonlinearity of the process in this regime also means that the optical alignment of the focusing objective is crucial. Even a small degree of defocus lead to a rapid decrease in the beam intensity on the surface which caused fluctuations in the diameter of the craters or moving below the damage threshold of the material.

The second ablation regime was observed when the pulse energy was increased

roughly by a factor of 5 above the material damage threshold, corresponding to the energy

fluence between 100 mJ/cm^2 and 1 J/cm^2. The craters in this regime were typically between

3 and 5 μm in diameter and 100 to 500 nm deep. A molten rim, similar to that seen in the

previous regime, was observed at the edge of the craters. The rim was more pronounced

around Si craters than around GaAs and InP craters. In addition, the surface quality of Si

craters was typically better than the surface quality of GaAs and InP craters. In general, the

craters were well defined and symmetric with no significant debris beyond the ablated area.

In both binary compounds frozen liquid droplets on the order of 100 nm were found on the

perimeter of the rim. With increasing pulse energy similar droplets were also found at the

bottom of the craters. Figure 4.3 shows SEM images and corresponding AFM profiles of the
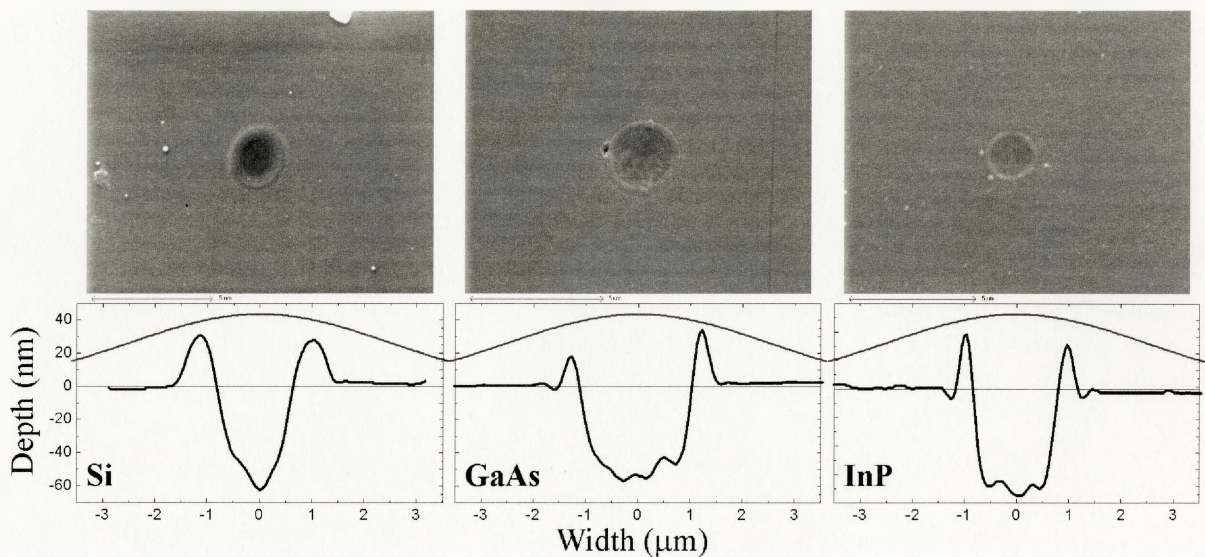
ablation features in the second ablation regime.

Figure 4.3: SEM images (top) and corresponding AFM profiles of ablation craters in the second ablation regime. The blue line indicates the position of the surface prior to irradiation; the red curve shows the Gaussian laser beam profile on the sample surface.

The ablation process in the second regime is essentially 100% reproducible and identical craters can be made across the entire length of the sample as shown in the figure below. Only small variations in the size and depth were observed due to the laser intensity instabilities.
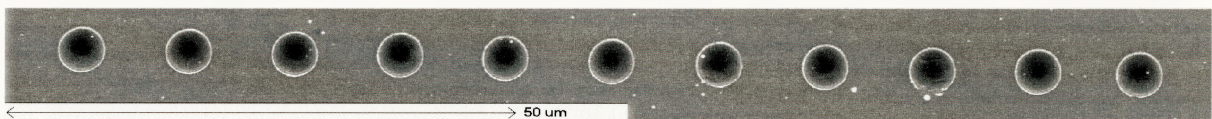
Figure 4.4: Ultrafast ablation of Si illustrating the reproducibility of the ablation process.

Optical alignment is not as critical as in the first ablation regime. Defocusing of the beam resulted in an increase of the spot size and therefore an increase in the size of the ablation craters. Aberrations such as astigmatism will lead to asymmetric craters and debris patterns.

The third ablation regime was observed when the pulse energy was increased beyond 500 nJ corresponding to the energy fluence above 1 J/cm². The diameter of the ablation craters was ~ 6 µm and ablation depth was on the order of 1 µm. In this ablation regime the surface morphology suggested a violent, explosive material removal process. A significant amount of debris resembling frozen liquid was found in the vicinity of the ablation craters. The random distribution of debris renders these patterns irreproducible. Figure 4.5 shows SEM images and corresponding AFM profiles of the ablation features in the third ablation regime.
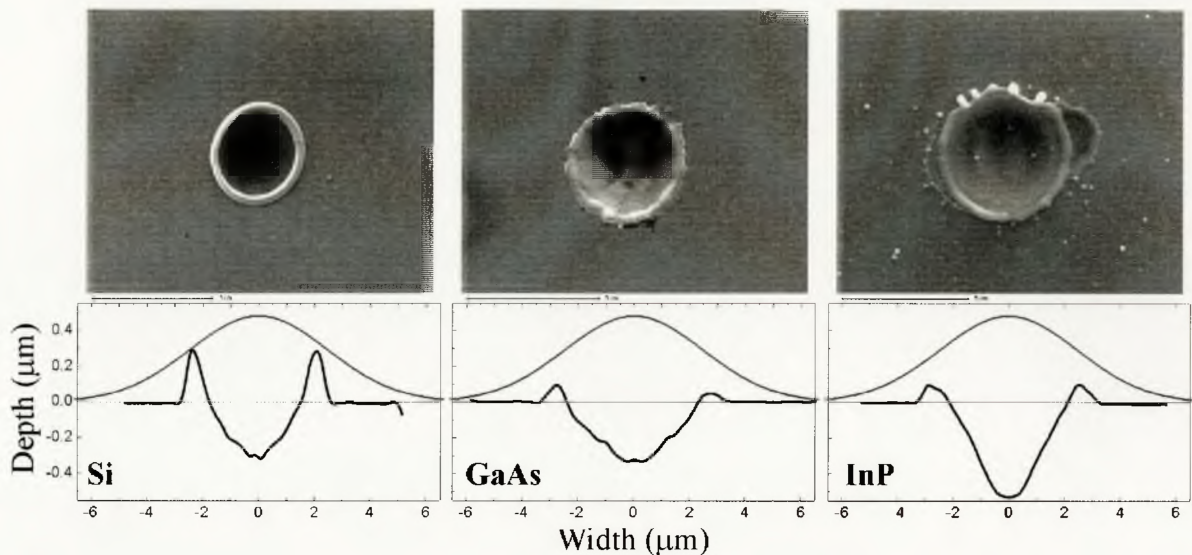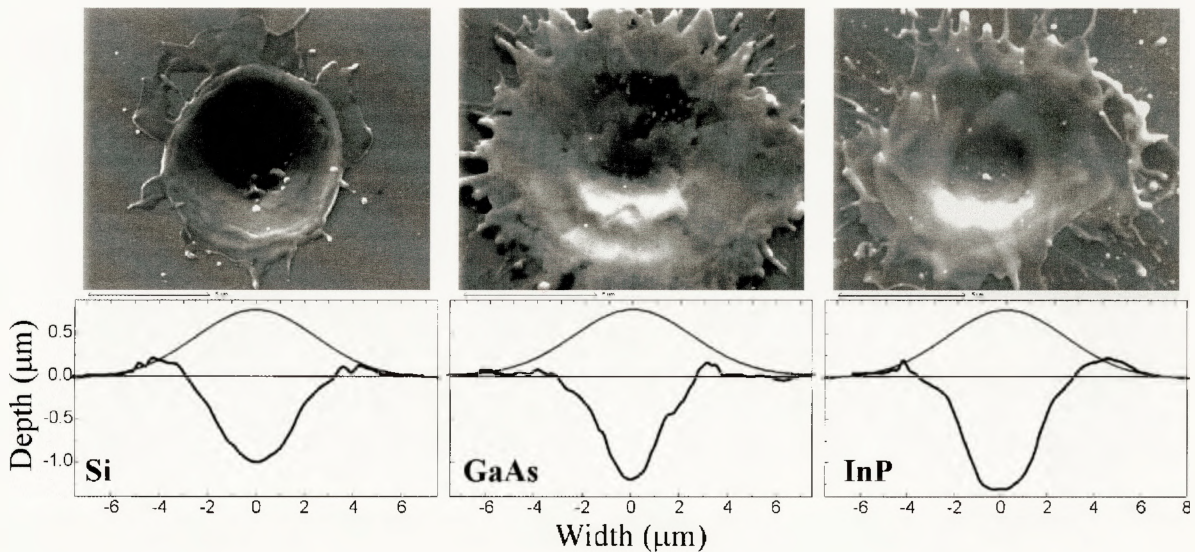

Figure 4.5: SEM images (top) and corresponding AFM profiles of ablation craters in the third ablation regime. The blue line indicates the position of the surface prior to irradiation; the red curve shows the Gaussian laser beam profile on the sample surface.

Intensities on the sample in this regime approach 10^{13} W/cm² and significant ionization of the material leads to the formation of a dense plasma. Emission from the generated plasma during sample processing stretches from visible all the way to the soft x-ray regime. In

previous studies presented in Chapter 3, we characterized x-ray emissions from solids irradiated in this intensity regime. X-rays are emitted as bremsstrahlung radiation and line emission depending on the atomic number of the target material and the excitation energy.

There are several challenges in TEM analysis of the ablation craters. In the case of craters near the damage threshold regime the biggest challenge is isolating information from the affected material. Single shot ablation craters near the damage threshold are only several nanometers deep while the thickness of the thinned substrate can be several tens of nanometers. Therefore a diffraction pattern from the affected area may be superimposed on a strong single crystal diffraction pattern from the substrate. By the same token EDX spectra will contain chemical information from the substrate and from the affected area. Sensitivity of the instrument may not be high enough to observe composition changes. Plan-view TEM analysis of the material craters in the highest fluence regime proved impossible due to difficulties in sample preparation. The high aspect ratio of the craters does not allow adequate back thinning of the entire crater without destruction of the area of interest. Thus, definite structural and compositional information about the frozen semiconductor is unavailable at this time. Further work will require more sophisticated cross sectional TEM analysis, which will be undertaken in the near future.

4.4.1 Ablation of Si

Figure 4.6 shows a sequence of SEM images of single shot ablation craters of Si produced by 130 fs, 794 nm pulses with pulse energy varied from 1.6 µJ (top left) to 20 nJ (bottom right). AFM profiles of 1.6 µJ, 820, 500, 200, 100 and 40 nJ are shown below the

SEM images. The z-axis of the plot is exaggerated; however all profiles are shown to the same scale.
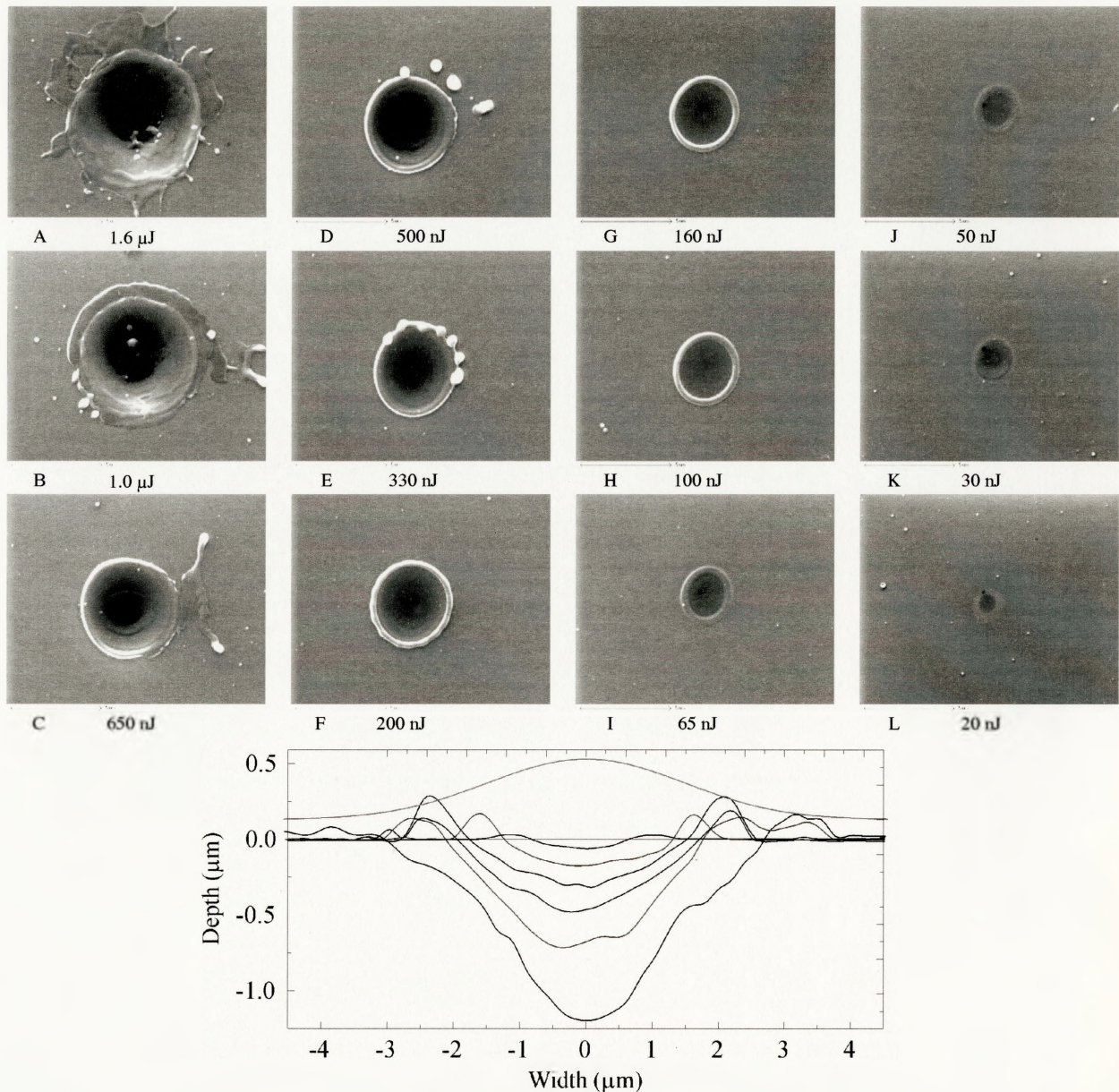
Figure 4.6: (top) Single shot ablation of Si with 794 nm, 130 fs pulses with pulse energies between 1.6 µJ to 20 nJ. The dimensions of all images are 15x12 µm, and all images are shown to the same scale. (bottom) AFM profiles of 1.6 µJ, 820, 500, 200, 100 and 40 nJ ablation craters shown to the same scale.

Under our experimental conditions, the damage threshold of Si was found to be 25 nJ ± 5 nJ. The corresponding energy fluence and intensity were 67 ± 10 mJ/cm^2 and (5 ± 1)· 10^{11} W/cm^2. The TEM diffraction patterns taken from the centre of the craters and from undamaged material in the vicinity of the crater consists of a strong single crystal pattern and very faint additional diffraction spots indicative of polycrystalline material. No other structural defects, such as dislocations or fractures, were found around any of the ablation sites.

Increasing the pulse energy leads to an increase in the size of the craters and the second ablation regime can be identified between pulse energies of 80 nJ and 400 nJ. The craters are typically between 3 and 5 μm in diameter and 150 to 500 nm deep for 80 nJ and 400 nJ pulses respectively. All craters feature a characteristic rim on the outer edge marking the boundary of the ablated zone. The rim is between 70 nm and 150 nm high for the pulse energies discussed above. The TEM diffraction patterns taken from the centre of craters correspond to a single crystal structure and they are identical to patterns taken from the pristine surface as shown in the figure below. The diffraction pattern from the rim reveals the presence of polycrystalline material.
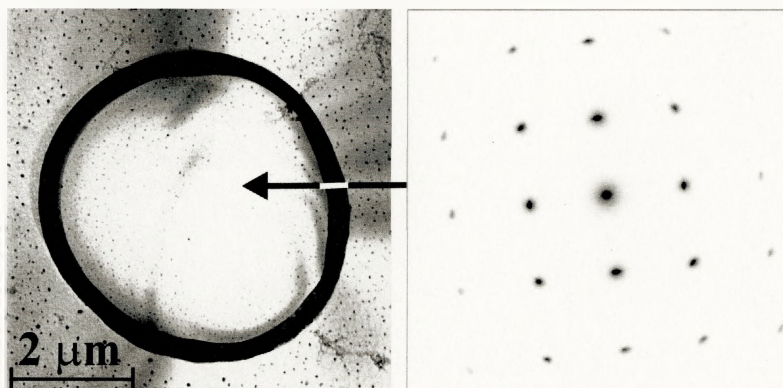
Figure 4.7: TEM image and diffraction pattern of Si crater in the second ablation regime.

With a further increase in the laser pulse energy, especially above 500 nJ, frozen droplets of Si, ~ 200 nm in diameter can be seen beyond the outer rim of the crater (Figure 4.6 D) and the surface morphology continues to degrade. Finally, in craters ablated by 1.6 µJ pulses, large debris patterns of frozen semiconductor material were found far beyond the rim. The volume of displaced semiconductor was measured to be 9 μm^3 and 3 μm^3 of debris was found on the surface within the vicinity of the crater.

4.4.2 Ablation of GaAs

Figure 4.8 shows a sequence of SEM images of single shot ablation craters in GaAs produced by 130 fs, 794 nm pulses with pulse energies between 1.6 µJ (top left) and 20 nJ (bottom right). AFM profiles of 1.6 µJ, 820, 500, 200, 100 and 40 nJ are shown below the SEM images.
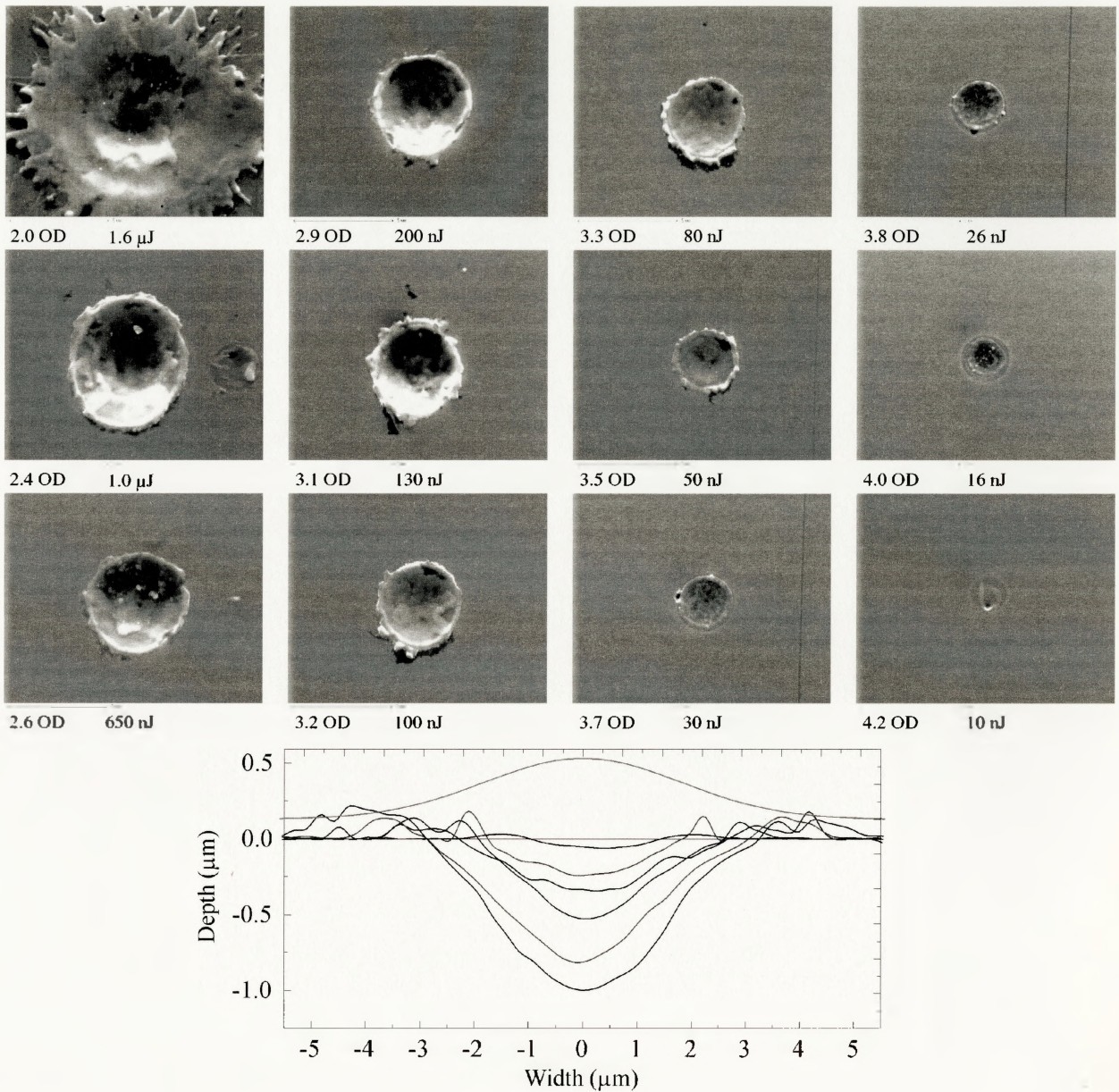
Figure 4.8: (top) Single shot ablation of GaAs with 794 nm, 130 fs pulses with a pulse energies between 1.6 µJ to 20 nJ. (bottom) AFM profiles of 1.6 µJ, 820, 500, 200, 100 and 40 nJ ablation craters shown to the same scale.

The damage threshold of GaAs was found to be 16 nJ ± 5 nJ. The corresponding energy fluence and intensity were 45 ± 10 mJ/cm^2 and $(3 \pm 1) \cdot 10^{11}$ W/cm^2. Near the damage threshold the ablated areas were less than 2 µm in diameter, and less than 50 nm deep, with

nanometer sized polycrystalline grains over the affected surface. The TEM diffraction pattern from the center of the craters consists of a strong single crystal pattern and a weaker pattern corresponding to a polycrystalline phase. The nanometer size polycrystalline grains can be seen in the TEM image of the damaged surface. The EDX analysis of the ablated area showed the same composition as the pristine substrate within the sensitivity of the spectrometer. The uncertainty in absolute composition measurements is ~ 10%.
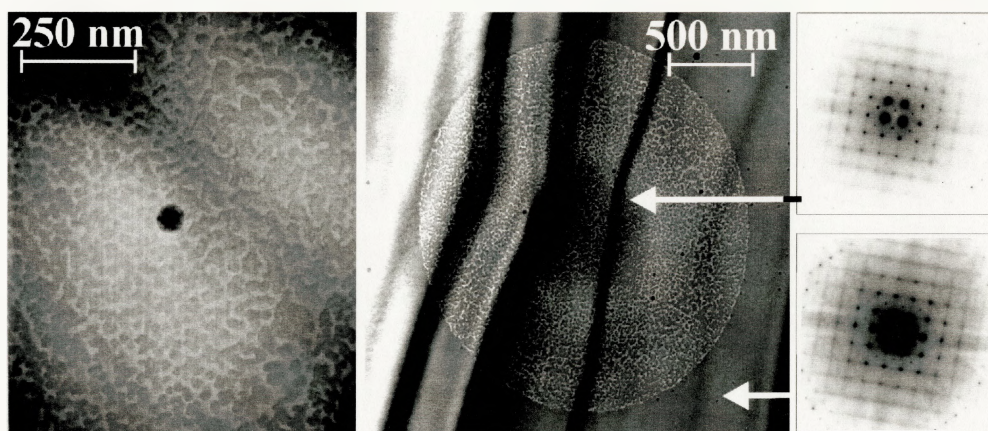
Figure 4.9: TEM image and diffraction patterns of GaAs crater in the near damage threshold regime.

In the intermediate pulse energy regime, between 80 nJ and 400 nJ, the size of the craters increases up to 5 μm, while the surface morphology degrades even further. The rim, which marks the ablation edge, was not as clearly defined as in the case of Si and was between 75 nm and 100 nm high for the pulse energies discussed above. Small polycrystalline droplets on the order of 100 nm were found on the perimeter of the rim. The compositions of the droplets, rim and the centre of the crater were still identical to the composition of the pristine substrate within the sensitivity of the EDX spectrometer.
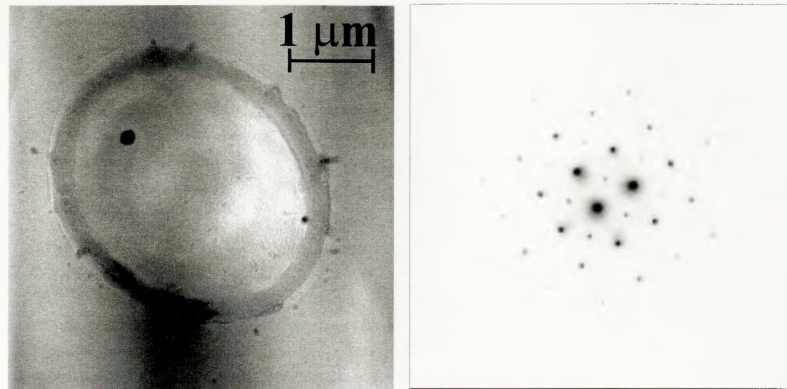
Figure 4.10: TEM image and diffraction pattern of GaAs crater in the second ablation regime.

In the highest pulse energy regime, above 500 nJ, definite evidence of melting and resolidification were observed. In the TEM image below, frozen droplets of material can be seen beyond the rim. The diffraction pattern from the rim, shown in the same diagram, indicates the presence of polycrystalline material. The polycrystalline grains range between 10 and 30 nm in size and can be seen in the higher magnification TEM image of the rim. At the maximum pulse energy of 1.6 µJ the volume of displaced semiconductor was 12 µm^3 and the extent of the damage was more extensive than in case of Si as can be seen in the SEM images. The volume of the debris found around the crater was 8 µm^3.
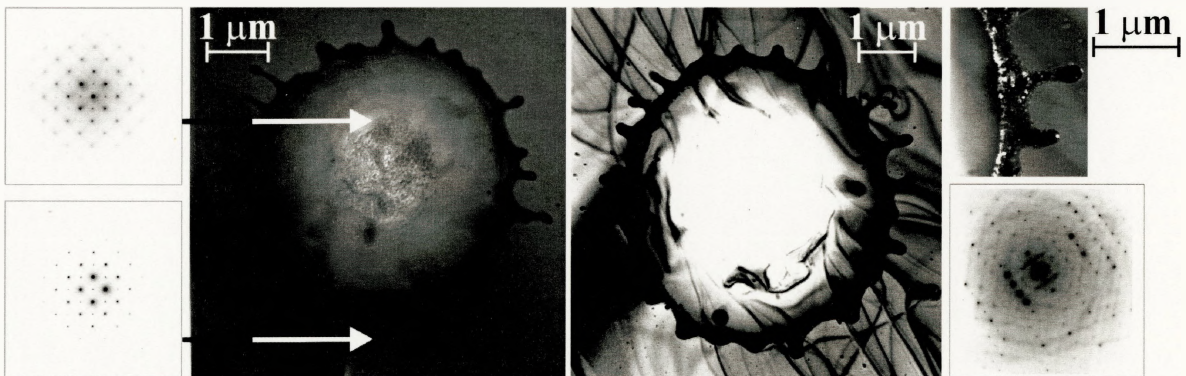
Figure 4.11 TEM image and diffraction pattern of GaAs crater in the second ablation regime.

4.4.3 Ablation of InP

Figure 4.12 shows a sequence of SEM images of single shot ablation craters produced by 130 fs, 794 nm pulses with the pulse energy varied from 1.6 µJ (top left) to 10 nJ (bottom right). AFM profiles of 1.6 µJ, 820, 500, 200, 100 and 40 nJ are shown below the SEM images.


A	1.6µJ	D	290 nJ	G	80 nJ	J	26 nJ
B	820 nJ	E	160 nJ	H	50 nJ	K	16 nJ
C	330 nJ	F	100 nJ	I	30 nJ	L	11 nJ
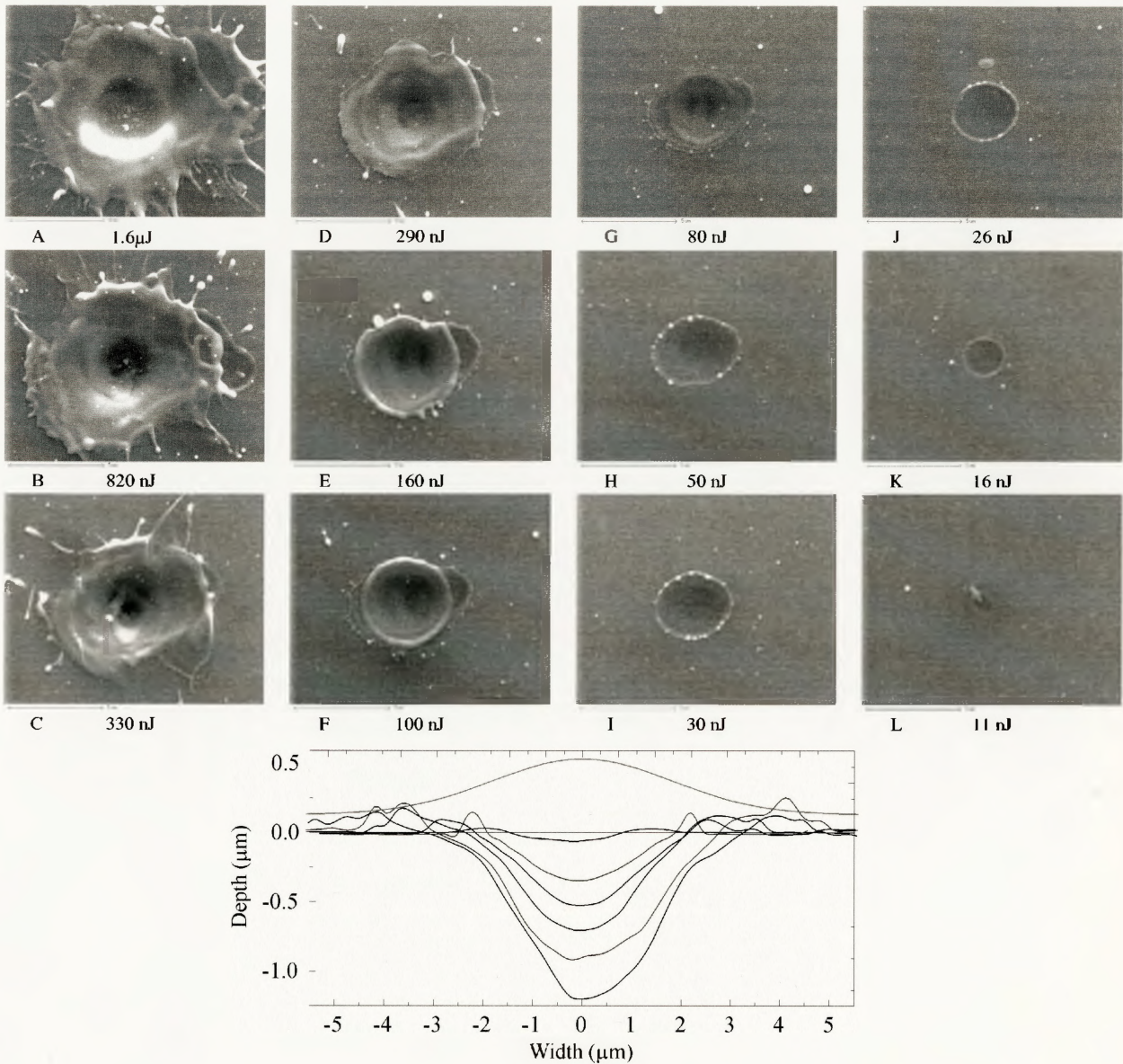
Figure 4.12: (top) Single shot ablation of InP with 794 nm, 130 fs pulses with pulse energies between 1.6 µJ to 10 nJ. (bottom) AFM profiles of 1.6 µJ, 820, 500, 200, 100 and 40 nJ ablation craters shown to the same scale.

The damage threshold of InP was found to be 10 nJ ± 5 nJ. The corresponding energy fluence and intensity were 30 ± 10 mJ/cm^2 and $(2 \pm 1) \cdot 10^{11}$ W/cm^2. Again, near the damage threshold, the ablated areas were less then 2 µm in diameter and less then 50 nm deep. In contrast to Si and GaAs TEM diffraction patterns from these areas feature full polycrystalline rings. Figure 4.13 shows a TEM image and a diffraction pattern from the area essentially at the damage threshold. The damaged spot is 500 nm in diameter and the polycrystalline InP grains can be seen over the affected surface. The grains were distributed without preferred crystal orientation and were typically 5-20 nm in diameter. A close-up of the polycrystalline grain is shown in the top left corner in the figure below. The composition of the affected region was the same as the composition of the pristine substrate.
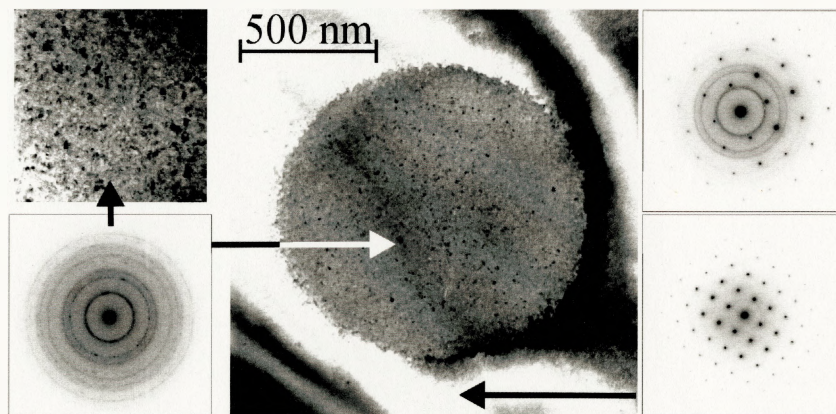
Figure 4.13: TEM image and diffraction pattern of InP irradiated near the damage threshold of the material. The pattern shown is 500 nm in diameter.

For pulse energies between 30 to 200 nJ the second ablation regime was observed. The craters were between 3-5 µm in diameter with molten rims marking the boundaries of the craters. The rims were between 50 nm and 120 nm high for the pulse energies mentioned

above. The TEM diffraction patterns from the centers of the craters reveal the presence of polycrystalline InP as well as underlying single crystal substrate as was seen in the low pulse energy craters. The 5-20 nm diameter polycrystalline grains were distributed over the entire surface within the boundary of the rim. In addition to the nanometer size polycrystalline grains, larger solidified material droplets, on the order of 100 nm, were found near the crater. EDX and energy loss spectroscopy analysis revealed that these were droplets of In. Diffraction patterns from such droplets indicated that the droplets were single crystal In. The rims of the craters were also composed of polycrystalline InP. Figure 4.14 shows TEM images and diffraction patterns from the indicated areas of the ablation crater.
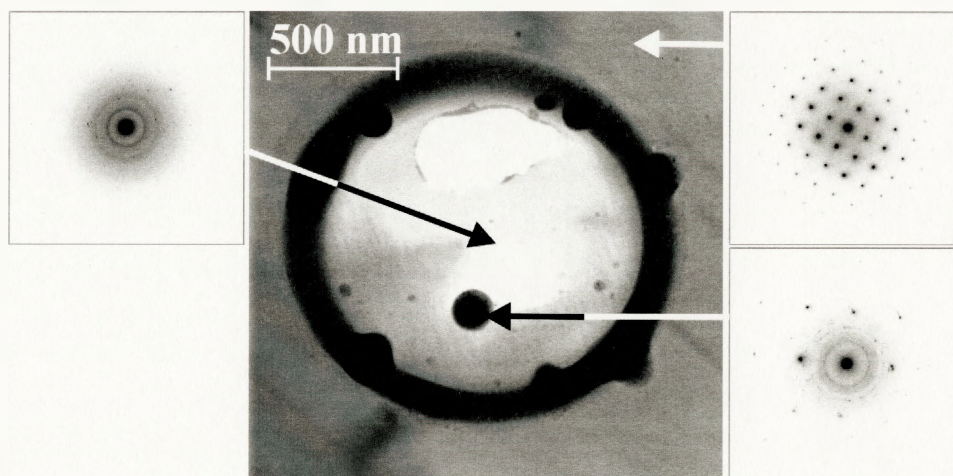
Figure 4.14. TEM analysis of InP ablation craters: image and diffraction patterns.

The third ablation regime is reached much quicker than in Si and even GaAs. An increase in pulse energy above 200 nJ resulted in a significant amount of debris being redeposited beyond the rim of the craters. At the pulse energy of 1.6 μJ the volume of

displaced semiconductor was measured to be 17 μm^3, but only 6 μm^3 of debris were found on the surface.

4.4.4 Ablation Yield

In order to gain a more quantitative picture of the process, **the ablation yields of Si, GaAs and InP** were compared by measuring the volume of material **removed per laser pulse** as a function of pulse energy. The volume measurements were performed **with the aid of** AFM by scanning an array consisting of craters, each one ablated **by a different pulse energy.** A mathematical routine was then used to fit a 2D function to the profile **of each crater and the** missing volume was calculated by integrating the volume below the surface. **The results of** the calculations are shown in the figure below on both linear and logarithmic scales.
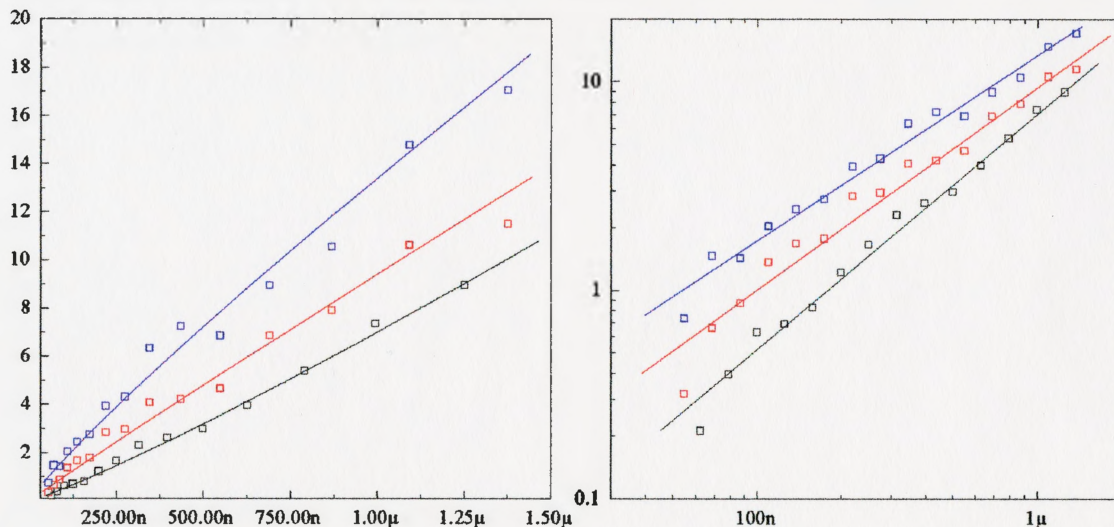
Figure 4.15: Volume of semiconductor (Si – black, GaAs – red and InP – blue) removed per laser pulse, linear scale (left) log scale (right).

The ablation yields per unit energy for Si, GaAs and InP are 7, 8 and 13 $\mu m^3/\mu J$ respectively. The linear dependence of the ablation process can be clearly seen. However, these numbers should not be taken as absolute since the volume of the resolidified and redeposited material cannot be easily measured. It would be interesting to compare the relative volumes of the material above and below the surface, but the acquired AFM scans lacked the resolution required to make accurate volume measurements, especially at the lowest pulse energy. High resolution scans of similar patterns are also planned for the near future.

The uncertainty in the damage threshold measurements arises mainly from the fact that the pulse energy is adjusted in finite steps, with an indexed neutral density filter set. In addition the uncertainty in the values of the neutral density filters at 800 nm is at most 5% (according to the company). In the near future the indexed filter wheel will be replaced by a combination of a thin film polarizer and a half-wave plate mounted in a precision rotation stage. This combination together with a calibrated photodiode allows continuous and very accurate pulse energy adjustments. The uncertainty in pulse energy calculations can also be attributed to the laser intensity fluctuations. The manufacturer's quote of 10% RMS intensity fluctuations were in agreement with the observed intensity instability. However, the intensity fluctuations tend to become more severe with the aging of the Merlin laser flash lamps. The uncertainty in the volume measurements is mainly caused by thermal drifts of the AFM during scan. Typically error margins are 0.5 μm in a 100 μm scan. Furthermore, scanning each crater separately would increase the accuracy of the volume measurements. However that process is extremely work intensive and impractical.

4.5 Discussion

The process of femtosecond laser ablation is very complicated and is still not well understood. It is therefore difficult to explain details of the resulting surface morphology, structure and material composition in terms of an existing model. However, it is instructive to view our results in light of recent time resolved ablation experiments and in terms of the physical properties of the semiconductors studied.

The ablation process begins with energy deposition. The semiconductors studied absorb strongly in the 800 nm region. The energy is absorbed by single and multiphoton excitation as well as by free carriers and other nonlinear processes. The nonlinear absorption channels are very important due to high laser intensities on the order of 10^{11} W/cm^2. The importance of nonlinear absorption is well illustrated by the fact that the difference in the damage threshold of Si and GaAs is only a factor of 0.8 despite the fact that linear absorption of GaAs at 800 nm is an order of magnitude higher than in Si. In contrast, during nanosecond ablation the damage thresholds of GaAs is 3 times lower than Si since the linear channel is the dominant absorption mechanism [59]. High laser intensities lead to excitation of a very dense electron-hole plasma. Estimates based on the reflectivity measurements suggest a carrier density on the order of 10^{22} cm^{-3} near the melting threshold [49], corresponding to roughly 10% of the total number of the valence electrons. Even higher carrier densities can be reached with increasing pulse energies or decreasing spot sizes. Exact details of the absorption dynamics such as bandgap renormalization, state filling and carrier diffusion have not been well characterized on femtosecond time scales and high

excitation intensities. The lattice dynamics and eventual fate of the material following femtosecond excitation depend critically on the absorbed energy. A number of groups [48-54] have reported two distinct ablation regimes: slow thermal melting and ultrafast non-thermal melting regimes separated by certain fluence thresholds, with the pulse width remaining constant.

In the fluence regime corresponding to the thermal melting, following excitation, carriers thermalize within the electron subsystem via ultrafast carrier-carrier scattering within tens of femtoseconds [60]. To a good approximation, a two temperature regime is established after excitation, comprising hot carriers and a cold lattice. Hot carriers transfer their energy to the lattice via a number of mechanisms including carrier-phonon scattering, carrier diffusion and Auger recombination. The semiconductor heats up and melts within several tens of picoseconds [49-53]. If the temperature of the melted layer is below the boiling temperature, the removal of material occurs by surface evaporation. If the material is superheated (heated above its boiling point), nucleation of gas bubbles can occur resulting in explosive boiling of the material. Species leaving the surface cause recoil pressure, on the order of the saturated vapor pressure, due to momentum conservation. The pressure exerted by the vapor on the remaining liquid in on the order of tens of MPa [47]. The recoil pressure forces the molten material outwards in a phenomenon known as liquid-phase expulsion. The material solidifies several nanoseconds after initial excitation [51,52].

In the fluence regime corresponding to the non-thermal ablation, the absorbed energy leads to excitation of extremely high free carrier concentrations causing destabilization of the

lattice; ultrafast melting is observed in less than 1 ps [49-53]. The temperature of the melted

volume can reach several thousand degrees, exceeding the critical temperature of the material

(see Table 4-1). During the melting phase, no significant expansion of material can occur

since the heating rate is much faster than the thermal expansion. Following melting, the

material undergoes phase explosion. Phase explosion can be considered as a collective

transformation from a solid phase directly to a homogenous phase consisting of vapour,

liquid droplets, and clusters of different size. Thus, irradiation of the material with ultrafast

pulses in this regime leads to very high pressures within the interaction volume and the

molten material can be regarded as a hot gas at high pressure. If we assume that the material

is heated to the critical temperature (T_c = 5159 K for Si), we can make a ballpark estimate of

the gas pressure based on the ideal gas law. For example, if we consider a Si crater ablated

by 200 nJ pulse, the volume of Si removed is V = 0.83 μm^3, corresponding to n = 7.0· 10^{-14}

moles of Si. By using P = nRT/V, where R is the gas constant we obtain pressures on the

order of 3 GPa. This rough estimate is on the same order of magnitude as values reported in

the literature [52]. This pressure drives a strong compression wave into the cold part of the

sample and the material is removed by recoil and hydrodynamic flow of hot fluid. The

material also solidifies within several nanoseconds after initial excitation [51,52].

The thresholds fluence for melting of Si and GaAs irradiated by 100 fs pulses

reported in the literature are: 150 mJ/cm^2 and 100 mJ/cm^2 for thermal melting, and

300 mJ/cm^2 and 150 mJ/cm^2 for non-thermal melting, [48-52]. To our knowledge the values

for InP were not reported. Under our experimental conditions the fluence at the damage

threshold of Si and GaAs was 67 mJ/cm^2 and 45 mJ/cm^2, roughly a factor of 2 lower than the values reported in the literature. The difference cannot be accounted for by the uncertainty in pulse energy measurements and the laser intensity fluctuations. An error in the spot size measurements is a very likely reason for the discrepancy. An error of 1 μm in the spot size ($2w_o$) values would result in factor of 2 difference in fluence calculations. The minimum step size of the positioning system used in the scanning knife setup is 0.5 μm. Therefore position errors on the order of a micron can be expected. The size of the damage features observed under SEM also suggests an overestimate of the spot size measurement. A thorough characterization of the optical system is currently under way.

Although the threshold behaviour of the transition from thermal to non-thermal melting has been observed and confirmed experimentally [48,54] it is important to realize that due to the Gaussian laser beam geometry ablation will most likely involve both regimes. Off axis areas experience a lower level of excitation due to spatial intensity variations and the smooth transition from non-thermal to thermal melting takes place over some specific distance. This transition was observed experimentally in spatially and temporally resolved reflectivity measurements [51]. The resulting surface morphology of the single shot ablation craters is therefore a result of thermal and non-thermal melting. In our experiments the evidence of thermal melting can be observed in all craters on the outer region and to a greater extent at low pulse energy near the damage threshold. At the damage threshold the affected areas are very shallow since the evaporation is a surface phenomenon. Increasing the pulse energy leads to higher temperatures in the interaction volume and increased crater depth

caused by the onset of explosive boiling. Within the sensitivity of our spectrometer, the composition of the crater surfaces in the cases of GaAs and InP was found to be same as the composition of the substrate. This fact suggests that there is no preferential loss of the more volatile constituent. Under thermodynamic equilibrium conditions, heating of GaAs and InP results in preferential loss of As and P and results in formation of Ga and In droplets on the surface. Segregation of binary compounds is also observed during nanosecond ablation [47,59]. In contrast, femtosecond irradiation results in highly non-equilibrium conditions with very rapid heating and cooling cycles. Instead of Ga and In droplets a thin layer of nanometer sized polycrystalline grains of GaAs and InP was found over the irradiated surface. It is still possible that the grains were Ga or In rich but beyond the sensitivity of the EDX spectrometer.

As the pulse energy increases, thermal melting occurs in the outside areas while the central part melts non-thermally and undergoes phase explosion. Redeposition of material during expansion is likely responsible for the surface irregular morphology of the craters. In the case of InP the presence of larger In droplets on the surface is not likely to be caused by material segregation. The possible process leading to formation of large In droplets is condensation of In upon expansion into vacuum. A segregation of binary compounds discussed earlier would result in nanometer size droplets densely distributed over the entire surface, whereas the observed drops were on the order of 100 nm and considerably spread out. If we consider ablated InP immediately after melting as a highly compressed homogenous mixture of In and P it is likely that nucleation of the less volatile component

takes place upon expansion. In and P have substantially different physical properties: the boiling points of In and P are 2346 K and 550 K respectively - therefore during rapid cooling In would be the first to condense and nucleate. The rapid heating and cooling cycles are also most likely responsible for the polycrystalline nature of the rim.

In addition to fundamental interest, the results presented contain valuable empirical information for practical consideration in femtosecond micromachining system. In particular, issues such as the damage threshold, the extent of material damage beyond the intended volume, as well as structural and chemical changes resulting from ablation, are of immediate interest. In the three materials measured, the damage threshold was highest in Si, followed by GaAs and InP. This is the expected result based on the physical and thermal properties of these materials, most notably the melting temperature. Above the ablation threshold a linear dependence of the ablation yield was observed with increasing pulse energy. Although a high ablation yield is desirable, higher pulse energies leads to a degradation in surface morphology. Pulse energies above 1 μJ lead to removal of volumes on the order of tens of cubic microns, but the material transport out of the ablated zone is a limiting factor. Substantial redeposition and resolidification of material during the cooling and expansion phases leads to poor surface morphology with large debris fields beyond the intended area. In some cases as much as 60% of the removed volume was found around the ablation craters, despite the fact that the experiments were performed under rough vacuum conditions. Improving vacuum conditions or even changing the geometry and the beam delivery to the sample may improve the situation. From a practical point of view the ability to machine

under ambient conditions is highly desirable; however in true micromachining a vacuum environment seems necessary.

Since the crater profiles reflect the intensity distribution in the focal plane, a flat top intensity profile is highly desirable in order to ensure uniform excitation of the material and minimize the thermal effects leading to the rim formation. A flat top profile can only be approximated if the spot size is much larger than the wavelength of light. As the spot size approaches ~λ the diffraction effects will dictate the intensity distribution in the focal plane. However, close to the diffraction limit, the high nonlinearity of the femtosecond ablation process can be exploited to produce features on a length scale below the diffraction limit. Our results clearly show that features much smaller than the spot size can be attained. By using a higher magnification focusing objective it is possible to produce sub-micron features. In recent experiments not discussed in this document, lines 20 μm by 250 nm have been achieved with a 20x microscope objective.

4.6 Summary

We have begun our micromachining research effort by studying single shot ablation of semiconductors. The semiconductors studied: Si, GaAs and InP, were irradiated with 130 fs pulses, centered about a wavelength of 794 nm. A microscope objective was used to focus the pulses between 2 μJ and 2 nJ in energy to a sub-10 μm spot size. The resulting surface morphology, structure and composition of the micron scale ablation features on the semiconductors were studied by electron microscopy and atomic force microscopy. We found that no sharp threshold in the surface morphology was observed with increasing pulse

energy, but three ablation regimes were identified based on the characteristic features of the ablation craters. In the first regime the ablation features were less than 2 μm in diameter and 50 nm deep. In all cases the features were much smaller then the spot size ($2w_o$ = 7 μm) indicating a high degree of nonlinearity. In the second regime the ablation craters were between 3 and 5 μm in diameter and up to 500 nm deep. The features were well defined with a minimum of surface debris and lateral damage. TEM analysis revealed essentially no crystal damage beneath and in the vicinity of the ablation craters. In the case of the binary semiconductors, 5-30 nm polycrystalline grains were found over the ablated surfaces. In the third ablation regime the craters were ~6 μm in diameter and a substantial amount of material was randomly redeposited around the craters. The results were discussed in terms of the existing state of knowledge of ablation dynamics. The implications for practical micromachining applications were also presented. Our work serves as an excellent starting point for further studies of micromachining and ablation of semiconductors and other materials in various pulse energy, wavelength and pulse duration regimes.

4.7 Appendix A: Physical Properties of Si, GaAs and InP

Table 4-1 Physical properties of semiconductors

Physical Properties	Si	GaAs	InP
Density (at 300 K) ρ – (g/cm^3)	2.33	5.32	4.81
Number of atoms per 1 cm^3	$5 \cdot 10^{22}$	$4.42 \cdot 10^{22}$	$3.96 \cdot 10^{22}$
Melting point T_m – (K)	1685	1513	1333
Specific heat capacity c_p – (J/g· K)	0.7	0.33	0.31
Thermal conductivity – (W/cm· K)	1.3	0.55	0.68
Thermal diffusivity – cm^2/s	0.8	0.31	0.372
Heat penetration depth – $l_t \sim 2(D \cdot \tau_p)^{1/2}$ (nm) during 130 fs pulse.	6.5	4.0	4.4
Critical temperature – (K)	5159	–	–
Bulk modulus – (dyne/cm^2)	$9.8 \cdot 10^{11}$	$7.53 \cdot 10^{11}$	$7.1 \cdot 10^{11}$
Optical absorption @ 800nm (cm^{-1})	$1.24 \cdot 10^{3}$	$1.17 \cdot 10^{4}$	$3.08 \cdot 10^{4}$

Chapter 5

Concluding Remark

During the past two years we have established an ultrafast laser laboratory, and as one of the projects undertaken, research in femtosecond laser micromachining. In preliminary experiments we have investigated x-ray generation during laser ablation of solids. The main goal of our experiments was to investigate the spectral nature and absolute dose rates of x-rays emitted during femtosecond laser micromachining. We have shown that relatively low energy pulses (~0.3 mJ) can excite x-rays with a high energy tail extending up to ~25 keV. The vast majority of the radiation was emitted below 10 keV with the radiation distribution approximated by a blackbody source at 8.9 MK (0.89 keV). Under our experimental conditions K line emission was observed from materials with Z<32. The emission exhibited a threshold-like dependence on the intensity. We have also measured the total x-ray dose rates during laser machining of various targets and observed dose rates as high as 10 mSv/h. Our results imply that appropriate precautions must be taken if similar laser systems are used in material processing applications. Our work also illustrates interesting possibilities for using modest size, high repetition rate systems as pulsed x-ray sources for spectroscopic and imaging applications.

The x-ray experiments and results presented in this document serve as a good basis for future investigations. Experiments planned for the near future include further characterization of the intensity dependence of the x-ray generation processes and correlation between ablation rates, quality of the material and total x-ray yields. We also suggested the use of x-ray emission as a characterization tool, during ablation of more complex substances, such as alloys, complex semiconductors and ceramics. Preliminary work will involve a spectroscopic study of x-ray emission during laser irradiation of binary metal alloys and semiconductors and analysis of the sensitivity of this process as on-line characterization tool.

After the preliminary x-ray experiments appropriate shielding and an enclosure were added to the micromachining setup. In the low pulse energy regime, below 2 μJ, we have then begun micromachining research by studying single shot ablation of semiconductors. The semiconductors studied: Si, GaAs and InP, were irradiated with 130 fs pulses, centered around a wavelength of 794 nm. A microscope objective was used to focus the pulses between 2 μJ and 2 nJ to a sub 10 μm spot size. The resulting surface morphology, structure and composition of micron scale ablation features were studied by electron microscopy and atomic force microscopy. We found that no sharp threshold in the surface morphology was observed with increasing pulse power, however three ablation regimes were identified based on the characteristic features of the ablation craters. In the first regime the ablation features were less than 2 μm in diameter and 50 nm deep. In all cases the features were much smaller than the spot size ($2w_o$ = 7 μm) indicating a high degree of nonlinearity. In the second regime the ablation craters were between 3 and 5 μm in diameter and up to 200 nm deep. The features were well defined with minimum surface debris and lateral damage.

TEM analysis revealed essentially no crystal damage beneath and in the vicinity of the ablation craters. In case of the binary semiconductors 5-30 nm polycrystalline grains were found over the ablated surface. In the third ablation regime the craters were ~6 μm in diameter and a substantial amount of material was randomly redeposited around the craters. The results were discussed in terms of the existing state of knowledge of ablation dynamics.

Our ablation investigations serve as an excellent starting point for further studies of micromachining and ablation of semiconductors and other materials. In the single shot ablation regime a very interesting parameter to explore is the wavelength of the excitation pulse. We have the capabilities to generate ultrashort pulses spanning the wavelength range from 3.0 μm to 300 nm through an optical parametric amplifier and associated nonlinear techniques. In semiconductors the ablation dynamics are expected to change dramatically as the wavelength crosses the bandgap. The effects of linear and nonlinear absorption can then be investigated with the wavelength and pulse energy as free parameters. In addition to wavelength, the excitation pulse duration can also be varied. Chirped pulse amplifier design provides access to pulse durations spanning several orders of magnitude while maintaining all the other laser parameters constant. We have ready access to pulse durations from 120 fs to 10 ns. By employing other nonlinear techniques, such as hollow capillary compression we can also compress our 120 fs pulses down to 10 fs. The experiments mentioned above are currently under preparation.

The next obvious extension of the current work involves investigating the effects associated with multiple shot exposures at high repetition rate. Ultimately most cutting and drilling applications will be performed with multiple shots. Thermal loading and

resolidification of the ablated material may result in a significant change of optical and mechanical properties of the material beyond the interaction regime. On a micron scale the extent of lateral damage is very important. In preliminary experiments we have used the polarization resolved photoluminescence imaging technique to image residual strain in grooves micromachined in InP and GaAs with femtosecond, picosecond and nanosecond pulses. The preliminary results clearly illustrate a reduction in magnitude and extent of material strain in grooves machined with femtosecond pulses. The results also demonstrate the possibility of the polarization resolved photoluminescence as a powerful diagnostic and evaluation tool of micromachinined structures.

In additional to semiconductors, femtosecond laser micromachining research can readily be extended to a wide range of materials including dielectrics, metals and ceramics. The absorption and ablation dynamics of these materials are significantly different and still not well understood. Dielectrics are particularly interesting since they are transparent in the near infrared and subsurface and bulk modification of these materials is possible. The exact nature of internal modification is currently a subject of intense research due to interesting possibilities in device fabrication. The possibility of direct writing of waveguides, gratings, diffractive elements and three dimensional storage media has captured the imagination of the optoelectronic and telecommunication industry.

With constant technological advances in the laser technology and increased deployment of femtosecond lasers in the industrial market, research on ablation dynamics, material properties and novel laser machining techniques will prove valuable to the industrial and scientific community.

References

[1] *Nonlinear fiber optics*, G. P. Agrawal, Academic Press (1995)

[2] *Ultrashort laser pulse phenomena*, J. C. Diels, W. Rudolph, Academic Press (1996)

[3] *60-fsec pulse generation from a self-mode-locked Ti:Sapphire laser*, D. E. Spence, P. N. Kean, W. Sibbet, Opt. Lett., **16**, 42 (1991)

[4] *Negative dispersion using pairs of prisms*, R. L. Fork, O. E. Martinez, J. P. Gordon, Opt. Lett., **9**, 150 (1984)

[5] *Negative group-velocity-dispersion using refraction*, O. E. Martinez, J. P. Gordon, R. L. Fork, J. Opt. Soc. Amer. **1**, 1003 (1984)

[6] *Compression of amplified chirped optical pulses.* D. Strickland, G. Mourou, Opt. Commun., **56**, 219 (1985)

[7] *Design of high-power ultrashort pulse amplifier by expansion and recompression*, O. E. Martinez, IEEE J. Quantum Electron., **QE-23**, 1385 (1987)

[8] *X-rays from Laser Plasmas*, I. C. Turcu, J. B. Dance, John Wiley, (1998)

[9] *Ultrafast Coherent and Incoherent X-ray Generation by Inner-Shell Atomic Processes Induced by <25 fs, > 1 J Pulses of High Power CPA Lasers*, C. Tóth, D. Kim, B. C. Walker, T. Guo, S. H. Son, C. W. Siders, A. Cavalleri, and C. P. J. Barty, Laser Phys. **10**, 513 (2000)

[10] *Time-resolved kiloelectron-volt spectroscopy of ultrashort plasmas*, J. C. Kieffer, M. Chaker, C. Y. Cote, Y. Beaudoin, H. Pepin, C. Y. Chien, S. Coe, G. Mourou, Appl. Opt. **32**, 4247 (1993)

[11] *Picosecond soft x-ray sources from subpicosecond laser-produced plasmas*, J. Workman, A. Maksimchuk, X. Liu, U. Ellenberger, J. S. Coe, C. Y. Chien, D. Umstadter, J. Opt. Soc. Am. B. **13**, 125 (1996)

[12] *Soft x-ray brilliance of femtosecond and picosecond laser-plasmas*, D. Altenbernd, U. Teubner, P. Gibbon, E. Foster, P. Audebert, J-P. Geindre, J. C. Gauthier, G. Grillon, A. Antoetti, J. Phys. B, **30**, 3969 (1997)

[13] *Hard x-ray emission from intense short pulse laser plasmas*, M. Schnurer, M. P. Kalashnikov, P. V. Nickles, Th. Schlegel, W. Sander, N. Demchenko, R. Nolte, P. Ambrosi, Phys. Plasmas **2**, 3106 (1995)

[14] *MeV X-ray generation with a femtosecond laser*, J. D. Kmetec, C. L. Gordon, J. J. Macklin, B. E. Lemoff, G. S. Brown, S. E. Harris, Phys. Rev. Lett. **68**, 1527 (1992)

[15] *Ultrafast X-Ray Absorption Probing of a Chemical Reaction*, F. Ráksi, K. R. Wilson, Z. Jiang, A. Ikhlef, C. Y. Côté, and J. -C. Kieffer, J. Chem. Phys., **104**, 6066 (1996)

[16] *Time-resolved soft x-ray absorption spectroscopy of silicon using femtosecond laser plasma x rays*, Hidetoshi N., Yoshinori G., Peixiang L., App. Phys. Let. **75**, 2350 (1999)

[17] *Anharmonic Lattice Dynamics in Germanium Measured with Ultrafast X-ray Diffraction*, A. Cavalleri, C. W. Siders, F. L. H. Brown, D. M. Leitner, C. Tóth, J. A. Squier, C. P. J. Barty, K. R. Wilson, K. Sokolowski-Tinten, M. Horn von Hoegen, D. von der Linde, and M. Kammler, Phys. Rev. Lett. **85**, 586 (2000)

[18] *Picosecond-milliangstrom lattice dynamics measured by ultrafast X-ray diffraction*, C. Rose-Petruck, R. Jimenez, T. Guo, A. Cavalleri, C. W. Siders, F. Ráksi, J. A. Squier, B. C. Walker, K. R. Wilson, and C. P. J. Barty, Nature, **398**, 310 (1999)

[19] *Elemental biological imaging by differential absorption with a laser-produced x-ray source,*. Tillman C, Mercer I., Svanberg S., J. Opt. Soc. Am. B (1996)

[20] *A 50-EW/cm² Ti:sapphire laser system for studying relativistic light-matter interactions*, B. C. Walker, C. Tóth, D. N. Fittinghoff, T. Guo, D. -E. Kim, C. Rose-Petruck, J. A. Squier, K. Yamakawa, K. R. Wilson, and C. P. J. Barty, Optics Express, **5**, 196 (1999)

[21] *Laser ablation and micromachining with ultrafast laser pulses,* X. Liu, D. Du, G. Mourou, IEEE JQE, **33**, 1706 (1997)

[22] See references in chapter 4

[23] *X-ray generation enhancement from a laser-produced plasma with a porous silicon target*, Tadashi N., Hidetoshi N., Hyeyoung A., App. Phys. Lett., **70**, 1653 (1997)

[24] *Soft x-ray emission produced by a sub-picosecond laser in a single- and double-pulse scheme*, J. F. Pelletier, M. Chaker, and J. C. Kieffer , J. App. Phys., **81**, 5980 (1997)

[25] *Laser ablation and micromachining with ultrafast laser pulses,* X. Liu, D. Du, G. Mourou, IEEE JQE, **33**, 1706 (1997)

[26] *Ultrashort pulse laser irradiation and ablation of dielectrics*, E. E. B. Campbell, D. Ashkenasi, A. Rosenfeld, Materials Science Forum, **301**, 123 (1999)

[27] *Laser induced breakedown as a function of pulse duration: from 7 ns to 150 fs*, D. Du, X. Liu, J. Squire G. Mourou, PIE Proc. Laser-induced Damage in Optical Materials: 1994,1995, **2428**, 422

[28] *Laser-induced damage in dielectrics with nanosecond to subpicosecond pulses*, B. C. Stuart, M. D. Feit, A. M. Rubenchik, B. W. Shore, M. D. Perry, Phys. Rev. Lett., **64**, 2248, (1995)

[29] *Femtosecond, picosecond and nanosecond laser ablation of solids*, B. N. Chichkov, C. Momma, S. Nolte, F. von Alvensleben, A. Tunnermann, Appl. Phys. A, **63**, 109, (1996)

[30] *Patterning of YBCO films by excimer-laser ablation*, Proyer S., Stangl E., Scheab P., Däuerle D., Simon P., Jordan C., Appl. Phys. A **58**, 471 (1994)

[31] *Ablation of polymer films by a femtosecond high-peak-power Ti:sapphire laser at 798 nm*, H. Kumagai, K. Midorikawa, K. Toyoda, S. Nakamura, T. Okamoto, M. Obara, Appl. Phys. Lett, **65**, 1850 (1994)

[32] *Ultrashort pulse lasers for hard tissue ablation*, J. N. Luiz, D. Silva, M. D. Feit, M. D. Perry, A. M. Rubenchik, B. C. Stuart, IEEE Journal of Selected Topics in Quantum Electronics, **2**, 790 (1996)

[33] *Femtosecond-pulse laser ablation of dental hydroxyapatite and single-crystaline fluoroapatite*, Krüger, J. Kautek, H. Newesely, Appl. Phys. A **69**, [suppl.], s403 (1999)

[34] *Femtosecond lasers for ultra-accurate surgery: application to corneal surgery*, T. Juhasz, F. H. Loesel, C. Horvath, R. M. Kurtz, G. Mourou, Ultrafast Phenomena XI, pp. 687, (1998)

[35] *Ablation of metals by ultrashort laser pulses*, S. Nolte, C. Momma, H. Jacobs, A. Tünnermann, B. N. Chichkov, B. Wellegehausen, H. Welling, J. Opt. Soc. Am. B, **14**, 2716 (1997)

[36] *Machining of submicron structures on metals and semiconductors by ultrashort UV-laser pulses*, P. Simon, J. Ihlemann, Appl. Phys. A, **63**, 505 (1996)

[37] *Machining of sub-micron holes using a femtosecond laser at 800nm*, P. Pronko, S. Dutta, J. Squire, J. Rudd, D. Du, Gl. Mourou, Opt. Commun., **114**, 106 (1995)

[38] *Nanostructuring with spatially localized femtosecond laser pulses*, S. Nolte, B. N. Chichkov, H. Welling, Y. Shani, K. Liberman, H. Terkel, Opt. Lett., **24**, 914 (1999)

[39] *Ultrafast-laser driven micro-explosions in transparent materials*, E. N. Glezer, E. Mazur, Appl. Phys. Lett, **71**, 882 (1997)

[40] *Photowritten optical waveguides in various glasses with ultrashort pulse laser*, K. Miura, Jianrong Qiu, H. Inouye, T. Mitsuyu, and K. Hirao, Appl. Phys. Lett, **71**, 3329 (1997)

[41] *Three-dimensional optical storage inside transparent materials*, E. N. Glezer, M. Milosavljevic, L. Huang, R. J. Finlay, H. Her, J. P. Callan, E. Mazur, Opt. Lett. **21**, 2023 (1996)

[42] *Three-dimensional optical memory using glass as a recording medium through a multi-photon absorption process*, J. Qiu, K. Mjura, K. Hirao, Jpn. J. Appl. Phys., **37**, 2263 (1998)

[43] *Fabrication of long-period fiber gratings by focused irradiation of infrared femtosecond laser pulses*, Y. Kondo, K. Nouchi, T. Mitsuyu, M. Watanabe, P. G. Kazansky, K. Hirao, Opt. Lett., **24**, 646 (1999)

[44] *Nonlinear Optical diagnostics of laser-excited semiconductor surfaces*, S. A. Akhmanov, N. I. Korteev, I. L. Shumay, Harwood Academic, (1989)

[46] *Pulsed Laser Processing of Semiconductors*, R. F. Wood, C. W. White, R. T. Young, Semiconductors and Semimetals, vol. 23, Academic, Orlando, (1984)

[47] *Laser processing and chemistry*, D. Bäuerle, Springer-Verlag, (2000) and references there in

[48] *Femtosecond time resolved surface structural dynamics of optically excited silicon*, C. V. Shank, R. Yen, C. Hirlimann, Phys. Rev. Lett, **51**, 900 (1983); *Time resolved study*

of laser induced disorder of Si surface, H. W. Tom, G. D. Aumiller, C. H. Brito-Cruz, Phys. Rev. Lett, **60**, 1438 (1988)

[49] *Ultrafast laser-induced order-disorder transitions in semiconductors*, Sokolowski-Tinten, J. Bialkowski, D. von der Linde, Phys. Rev. B, **51**, 14186 (1995-II)

[50] *Femtosecond melting and ablation of semiconductors studied with time of flight mass spectroscopy*, A.Cavalleri, K. Sokolowski-Tinten, J. Bialkowski, M. Schreiner, D. von der Linde, J. App. Phys, **85**, 3301 (1999)

[51] *Thermal and nonthermal melting of gallium arsenide after femtosecond laser excitation*, K. Sokolowski-Tinten, J. Bialkowski, M. Doing, A, Cavalleri, D. von der Linde, Phys. Rev. B, **58**, R11 805 (1998)

[52] *Transient States of Matter during Short Pulse Laser Ablation*, K. Sokolowski-Tinten, J. Bialkowski, M. Doing, A, Cavalleri, D. von der Linde, A. Oparin, J. Mayer-ter-Vehn, S. I. Anisimov, Phys. Rev. Lett. **81**, 224 (1998)

[53] *Picosecond-milliangstrom lattice dynamics measured by ultrafast x-ray diffraction*, C. R. Petruck, R. Jimenez, T. Guo, A. Calalleri, C. W. Siders, F. Raksi, J. A. Squire, B. C. Walker, K. R. Wilson, C. P. J. Barty, Nature **398**, 310, (March 1999)

[54] *Anharmonic Lattice Dynamics in Germanium Measured with Ultrafast X-ray Diffraction*, A. Cavalleri, C. W. Siders, F. L. H. Brown, D. M. Leitner, C. Tóth, J. A. Squier, C. P. J. Barty, K. R. Wilson, K. Sokolowski-Tinten, M. Horn von Hoegen, D. von der Linde, and M. Kammmler, Phys. Rev. Lett. **85**, 586 (2000)

[55] *Time dependence of the laser-induced femtosecond lattice instability of Si and GaAs: Role of longitudinal optical distortions*, P. Stampfli, K. H. Bennemann, Phys. Rev. B, **49**, 7299 (1994)

[56] *Ultrashort pulse laser ablation of silicon: an MD simulation study*, R. F. W. Herrmann, J. Gerlach, E. E. B. Campbell, Appl. Phys. A, **66**, 35, (1998)

[57] *Pulsed laser evaporation: equation-of-state effects*, S.I. Anisimov, N.A. Inogamov, A.M. Oparin, B. Rethfeld, T. Yabe, M. Ogawa, V.E. Fortov, Appl. Phys. A. **69**, 617 (1999)

[58] *Expansion of matter heated by an ultrashort laser pulse*, N. A. Inogamov, Yu. V. Petrov, S. I. Aanismov, A. M. Oparin, N. V. Shaposhnikov, D. von der Linde, J. Mayer-ter-vehn, JETP Lett. **69**, 310 (1999)

[59] *Laser ablation process imaged by high-speed reflection electron microscopy*, F. Heinricht, O. Bostanjoglo, Appl. Surf. Sci., **54**, 244, (1992)

[60] Initial thermalization of photoexcited carriers in GaAs studied by femtosecond luminescence spectroscopy, T. Elsaesser, J. Shah, L. Rota, P. Lugli, Phys. Rev. Lett. **66**, 1757 (1991)